NANOSTRUCTURE ENHANCED THERMOELECTRIC PROPERTIES IN SNSE AND SNTE THIN FILMS

SUEN CHUN HUNG

MPhil

The Hong Kong Polytechnic University

2018

The Hong Kong Polytechnic University

Department of Applied Physics

Nanostructure Enhanced Thermoelectric Properties in SnSe and SnTe Thin Films

SUEN Chun Hung

A thesis submitted in partial fulfillment of the requirements for the degree of Master of Philosophy

August 2017

CERTIFICATE OF ORIGINALITY

I hereby declare that this thesis is my own work and that, to the best of my knowledge and belief, it reproduces no material previously published or written, nor material that has been accepted for the award of any other degree or diploma, except where due acknowledgement has been made in the text.

_____ (Signed)

SUEN Chun Hung (Name of student)

Abstract

The consumption of energy increases continuously because of the growth of economy, industry and global population; meanwhile there is large amount of heat dissipation lost as waste energy. This problem presents from large-scale, such as the hot fluids including exhaust gases in power plants, to small-scale such as the hot spots with higher power density in the microprocessors. There is a need for developing appropriate ways to collect or reuse the dissipated heat, among them thermoelectric devices can address the problem with advantages of compact, reliable and produce no pollutants. Throughout the development of thermoelectricity, different approaches for enhancing thermoelectric figure of merit were proposed and investigated, and different materials were discovered to have extraordinary thermoelectric properties. Among these materials, SnSe single crystal exhibits ultralow thermal conductivity and very high figure of merit. SnTe is another candidate who has similar crystal and electronic band structure as PbTe which is a well-known good thermoelectric material but contain toxic lead. Both SnSe and SnTe show potential to be prominent thermoelectric materials.

In this work, two approaches enhancing the thin film thermoelectric figure of merit are investigated, namely *grain size reduction* and *multilayered structure*. SnSe thin films with different grain sizes are deposited, and their structural and thermoelectric characteristics are studied. SnTe and multilayered thin films composed

of SnSe and SnTe are also deposited to investigate the difference of structural and thermoelectric properties between them.

SnSe thin films are fabricated by pulsed-laser deposition at normal angle and glancing angle on different substrates. With glancing angle deposition, nanopillar structure is achieved in the SnSe film, presenting smaller grain size than that of the normal angle grown film. The Seebeck coefficient of the nanopillar structured film is enhanced with the power factor attains 18.5 $\mu W cm^{-1} K^{-2}$ due to the energy barrier scattering.

SnTe film and a multilayered thin film with six alternating layers of SnSe and SnTe are deposited, and a layer-by-layer growth is demonstrated in the multilayered film. The studies in thermoelectric properties for the multilayered film also show an improvement in Seebeck coefficient compared to the SnTe film, leading to an increased power factor.

The investigations done in this work revealed the effect of grain size and multilayered structure to the thermoelectric properties of SnSe and SnTe thin films. These results provide strategies for enhancing figure of merit of thermoelectric thin films.

List of Publications

Journal Articles

1. Suen, C. H., Shi, Dongliang, Su, Yu, Zhang, Zhi, Chan, Cheuk Ho, Tang, Xiaodan, Li, Y., Lam, Kwok Ho, Chen, Xinxin, Huang, B. L., Zhou, X. Y., Dai, Ji-Yan. Enhanced thermoelectric properties of SnSe thin films grown by pulsed laser glancing-angle deposition. *Journal of Materiomics* **3**, 293-298 (2017)

Acknowledgements

I would like to express my sincere appreciation to my supervisor Prof. J. Y. Dai for his constructive suggestion, encouragement, patient help and continuous support over my whole period of research work. With his broad knowledge and academic insight, I can finish my M.Phil study smoothly, quickly and successfully.

In addition, I would like to extend my thanks to my group mates and friends, especially Mr. Cheuk Ho Chan, Mr. Chi Man Wong, Miss Hei Man Yau and Mr. Fan Zhang, for their friendship, useful help and valuable discussion in my experiments.

I also appreciate Dr. K. H. Lam and D. L. Shi from the department of Electrical Engineering, Prof. B. Huang, Y. Su and Y. Li from Hong Kong University of Science and Technology and Mr. Kai Hong Ho for the technical support and discussion.

Moreover, I gratefully acknowledge the Materials Research Centre of the Hong Kong Polytechnic University for the provided technical support, without their support, my study cannot be finished.

Finally, I am grateful to my family for their endless love and encouragement.

This thesis is dedicated to all of them.

Table of Contents

List of Figures

Chapter 1 Introduction

Due to the rapid growth of economy, industry and global population, the energy demand is continuously ascending. In a research done by the United States Energy Information Administration in 2017[1], the need of energy in the state is increasing over decades, and it can be foreseen that in the future the consumption will keep growing as shown in Figure 1.1, this situation is similar all over the world. To handle with the huge amount of energy demand, the energy is now mainly provided by fossil fuels including natural gas, coal, and oil.

These energy sources typically are burned and converted to heat, after that the heat energy is used directly or converted to useful mechanical work through thermodynamic processes. These systems usually take heat energy as the first step of energy conversion; however a large amount of heat is leaked from the hot fluids including exhaust gases, and the surface of the hot parts such as engines through conduction, convection and radiation. According to a research done by Energetics[2], the amount of heat dissipated to the surroundings can range up to 50% of energy input.

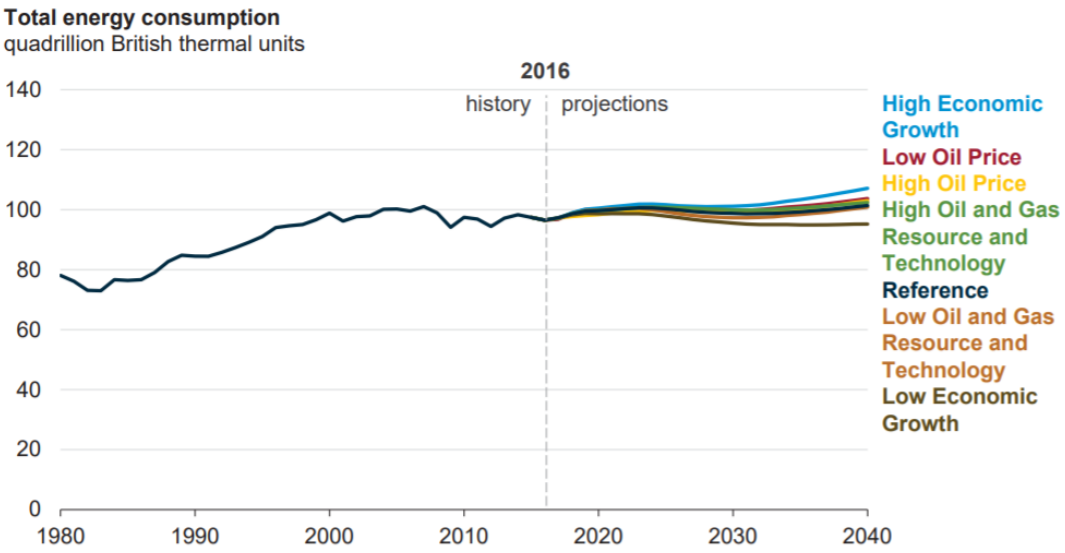

Figure 1.1. Prediction of total energy consumption up to 2040[1].

Not only in industrial region, heat dissipation occurs also in electronic devices such as IC chips. Nowadays there is a high demand on microprocessors, especially in some industries like computer, instrumentation and communication. In these microprocessors the power density is estimated to be 100 W/cm^2, and as the transistor density in an integrated circuit (IC) unit is continuously increasing deduced by Moore's law[3], the power density inside a microprocessor is expected to be increasing. In an IC unit, the regions with the higher power density are usually described as "hot spots", and these hot spots mainly cause the fatal thermal failure. To handle the uneven power dissipation in place and time regimes, providing site specific and on-demand cooling becomes a strategy[4].

To provide local cooling, or even reuse the waste heat from small-scale components like IC units to large-scale systems such as exhaust gas pipes in power plants, thermoelectric (TE) device is a good candidate to address the problem. TE devices are

systems without working fluids or moving parts, which make them compact, reliable and noise free; also by making use of TE effect, TE devices produce no pollutants. However, because of the interdependence between the physical properties which are discussed in the later section, the bulk materials' figure of merit, zT, which is an indicator of thermoelectric performance, was limited to around one at room temperature. Later in 1993, it was proposed that in low dimensional structures such as quantum wells, the zT can be greatly enhanced because of the confinement of carrier from 3D to 2D, and the phonon scattering by the interface between layers[5,6]. After this prediction, research interest about experiments and modeling on low dimensional TE materials was aroused.

1.1 Historical development of TE effects

TE effects can be separated into Seebeck effect, Peltier effect and Thomson effect. From 1821 to 1851, knowledge about thermoelectricity experienced an important development. The first effect named Seebeck effect was discovered in 1821, a German physicist Thomas Johann Seebeck discovered that for two dissimilar conductors, if they form a closed loop with one of the junctions heated, a nearby compass needle will be deflected. He erroneously reported this discovery in 1823 that the interaction was a magnetic phenomenon, although it is a TE effect with the wisdom of hindsight[7]. After 12 years, Peltier observed that when a current passes through a junction between two dissimilar conductors, heat is absorbed or generated at the junction depending on the

direction of the current[8], so this phenomenon was named as Peltier effect. In 1951, W. Thomson predicted the third TE effect, the Thomson effect, by establishing the relationship between Seebeck and Peltier coefficients, this effect reveals that given a single homogeneous conductor in the presence of a temperature gradient, the conductor will absorb or release heat when a current passes along the conductor depending on the direction of the current flow[9].

1.2 General principles of thermoelectricity

When a thermal gradient is applied to the two ends of a TE material with single type of carrier, the mobile charge carriers, which are electrons (e^-) or holes (h^+), tend to diffuse from the hot end to the cold end carrying charge and heat. The varied carrier distribution between the two ends during the diffusion, consequently, creates an electrostatic potential difference, which is known as Seebeck effect. Reversely, the mobile carriers can be driven from one end of TE material to the other end if a current is applied. This is named as Peltier effect.

Figure 1.2 illustrates the circuits of thermoelectric generator (TEG) and thermoelectric cooler (TEC) by utilizing Seebeck and Peltier effects respectively. They consists of two couples namely a p-type and an n-type couple; and the two couples are connected electrically in series and thermally in parallel. In the p-type couple the free charge carriers are holes, whereas electrons are the mobile carriers in n-type material. As shown in Figure 1.2a, when heat is applied to the top of a TEG, the mobile charge

carriers diffuse from the hot junction to the cold junction, subsequently the heat loaded by carriers can be ejected from the cold junction to an additional heat sink. Notably the diffusion of the two types of carrier still results in one direction of current flow. In a Peltier cooler (Figure 1.2b), a DC power supply drives the carriers through the thermocouple, and that the carriers flow from the bottom of TEC to the top, carrying the heat. To make the device work, a heat sink should be applied to the hot junction.

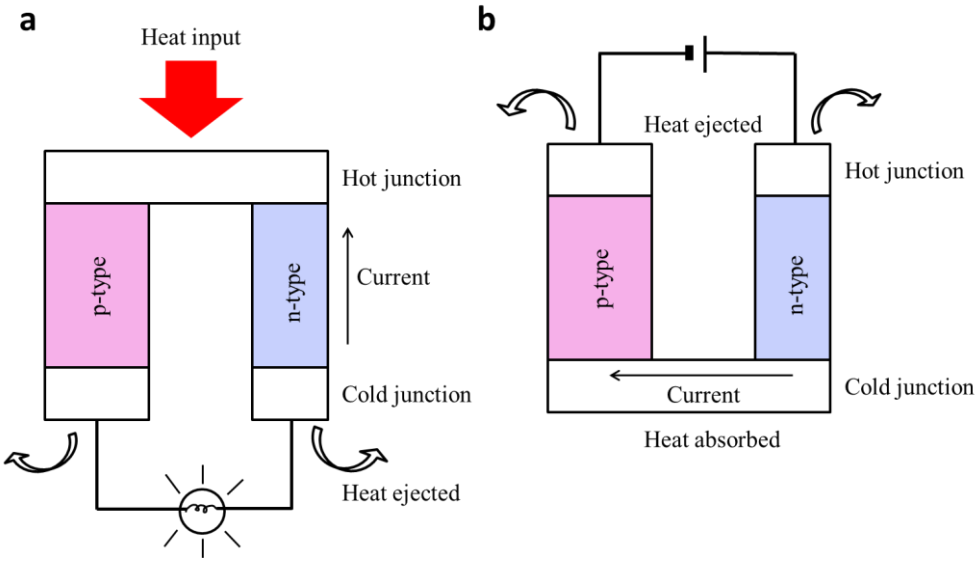

Figure 1.2. Illustration of (a) a thermoelectric generator circuit and (b) a thermoelectric cooler circuit.

When many pairs of thermoelectric circuit are electrically connected, a thermoelectric module can be realized, as shown in Figure 1.3. Da Silva *et al.*[10] implemented a thin film thermoelectric cooler (TFTEC). The TFTEC contained up to 300 pairs of thermocouples, where Bi_2Te_3 was the n-type couple and Sb_2Te_3 for the p-type couple. The columns of thermocouple were 4 μm high and the cross-sectional areas were

down to 7 x 7 μm^2. Each column was connected by Cr/Au and Ti/Pt films with 200 nm and 20 nm thick, respectively. Figure 1.4 shows the structure and Scanning Electron Microscope (SEM) images of the TFTEC.

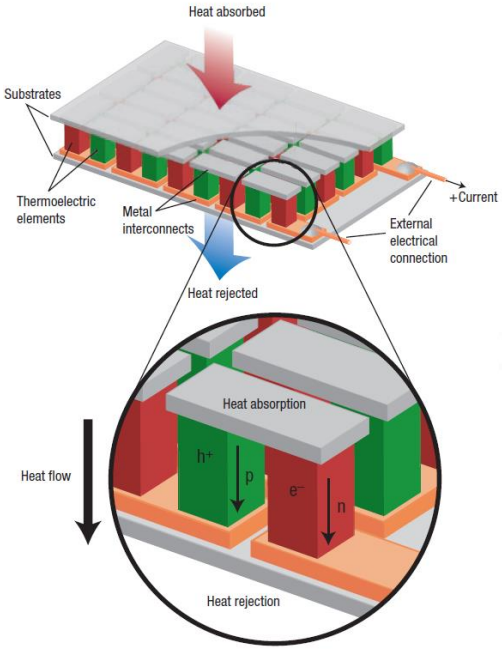

Figure 1.3. Illustration of a thermoelectric module.[11]

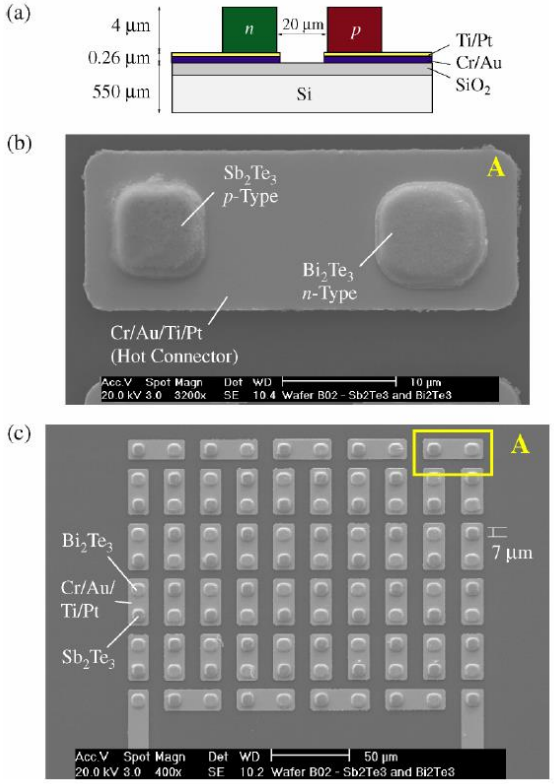

Figure 1.4. TFTEC with Bi_2Te_3 as the n-type couple and Sb_2Te_3 as the p-type couple. (a) Schematic of the TFTEC structure showing thicknesses of the films. (b) SEM image of one of the couple. (c) SEM of the TFTEC with 50 thermoelectric pairs.[12]

The small TFTEC can be used in Thermal Interface Material (TIM). Figure 1.5 shows an illustration of an electronic component, TFTEC forms a TIM between the component and the heat sink, nanoparticles are added into the TIM to enhance the thermal conductivity of TIM. When heat is generated in the electronic component, it will be transfer to the TIM. The TFTEC here acts as an active cooler, and by applying voltage to the TFTEC, it will forward the heat from TIM to heat sink.

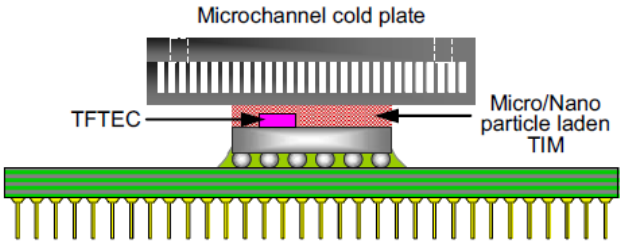

Figure 1.5. Illustration of thermal interface material sandwiched by electronic component and heat sink.[13]

1.3 Factors evaluating a TE material

Upon the discoveries of TE effects, the factors affecting the performance of a TE material remained unclear until a satisfactory TE theory was proposed. Altenkirch[14,15] showed that a potential TE material should possess a large Seebeck coefficient and a high electrical conductivity to minimize joule heating. In addition the material should retain a low thermal conductivity to maintain the temperature difference between the hot and cold junctions. He established a dimensionless figure of merit zT, $zT = \sigma\alpha^2 T/(\kappa_L + \kappa_e)$, where σ, α, T, κ_L and κ_e represent electrical conductivity, Seebeck coefficient, temperature in Kelvin, lattice thermal conductivity and electronic thermal conductivity respectively. Moreover, zT consists of two parts including electronic part and thermal part, where the electronic part, $\sigma\alpha^2$, is called the power factor, and thermal part is the sum of lattice and electronic thermal conductivities. In the following, those physical properties contributed to zT are introduced specifically.

1.3.1 Seebeck coefficient

Seebeck coefficient is also known as thermopower with SI unit of V/K or more often $\mu V/K$, and it can be measured by the ratio between the induced Seebeck voltage and the temperature difference across the TE material. The mathematical presentation of Seebeck coefficient is given by:

$$\alpha_v = -\frac{\nabla_r \varphi_v}{\nabla_r T} \tag{1.1}$$

where $\nabla_r \varphi_v$ is the spatial gradient of chemical potential and $\nabla_r T$ is the spatial temperature gradient, ν denotes whether the mobile carrier is electron or hole. The short circuit condition of current density in terms of chemical potential and temperature gradient is expressed as:

$$j_\nu = -s_\nu \mu_\nu \nu \nabla_r \varphi_\nu - \mu_\nu \nu \frac{k_B}{q}\left(\frac{5}{2} - ln\frac{\nu}{N_{C,V}}\right)\nabla_r T = 0 \tag{1.2}$$

Assume the mobile carriers are in local thermal equilibrium with lattice, such that the carrier temperature is equal to the lattice temperature:

$$T_\nu = T_L = T \tag{1.3}$$

By applying equations 1.3 and 1.2 into 1.1, a generalized definition of Seebeck coefficient is obtained:

$$\alpha_v = s_\nu \frac{k_B}{q}\left(\frac{5}{2} - ln\frac{\nu}{N_{C,V}}\right) \tag{1.4}$$

Specifically, the Seebeck coefficients of n-type material and p-type material are presented respectively as:

$$\alpha_n = -\frac{k_B}{q}\left(\frac{5}{2} - ln\frac{n}{N_C}\right) \tag{1.5}$$

$$\alpha_p = \frac{k_B}{q}\left(\frac{5}{2} - ln\frac{p}{N_V}\right) \tag{1.6}$$

In equations 1.5 and 1.6, k_B is the Boltzmann constant, q is charge of electron, n and p denote the carrier concentration of electron and hole, N_C and N_V represent the effective density of states of conduction band and valence band, respectively. Note that the equations do not involve scattering terms, so a term r_v denoting the relaxation time of different scattering mechanisms can be introduced:

$$\alpha_n = -\frac{k_B}{q}\left(\frac{5}{2} + r_n - ln\frac{n}{N_C}\right) \tag{1.7}$$

$$\alpha_p = \frac{k_B}{q}\left(\frac{5}{2} + r_p - ln\frac{p}{N_V}\right) \tag{1.8}$$

1.3.2 Electrical conductivity and thermal conductivity

Electrical conductivity of a material is related to the carrier density and the carrier mobility, with unit of S/cm. For an isotropic conductor, the electrical conductivity can be presented as:

$$\sigma = \frac{1}{\rho} = nq\mu_n + pq\mu_p \tag{1.9}$$

where σ, ρ, n, q, μ_n, μ_p and p are electrical conductivity, electrical resistivity, electron concentration, electron charge, electron carrier mobility, hole carrier mobility and hole concentration, respectively. In addition, if n>>p or p>>n, σ can be simplified as $nq\mu_n$ or $pq\mu_p$.

Mobility is associated with carrier effective mass and scattering mechanisms, the mathematical expression of it is:

$$\mu = \frac{q\tau}{m^*} = \frac{q\lambda_c}{m^* v} \tag{1.10}$$

where τ, m^*, λ_c and v are carrier mean free time, effective mass, carrier mean free path and group velocity of different scattering process, respectively. Based on equations (1.9) and (1.10) mobility decreases when the effective mass of carrier increases; to obtain a high electrical conductivity, the material should have small effective mass and high carrier concentration.

Thermal conductivity κ represents how well the material conducts heat, and it is the sum of electronic thermal conductivity κ_e and lattice thermal conductivity κ_L:

$$\kappa = \kappa_e + \kappa_L \tag{1.11}.$$

Electronic thermal conductivity is related to the heat transfer by electrons and holes, and moreover, it forms a relationship with electrical conductivity through the Wiedemann-Franz law[11,16,17]:

$$\kappa_e = L_0 \sigma T = L_0 ne\mu T \tag{1.12}$$

In the equation L_0 is Lorenz number. In vacuum and solids, L_0 are $2.4 \times 10^{-8} (J^2 K^{-2} C^{-2})$ for free electrons, at that time electrons only undergo elastic collisions.

Lattice thermal conductivity is the ability of heat conduction by phonon, it can be expressed as[11,16,17]:

$$\kappa_L = \frac{1}{3} C_p v_\varphi \lambda_\varphi \tag{1.13}$$

where C_p, v_φ and λ_φ stand for the specific heat, phonon velocity and phonon mean free path respectively. It is complicated to solve equation (1.13) because a spectrum of phonon needs to be calculated with wide range of frequencies and mean free paths, as well as different scattering mechanisms[11].

1.4 Tradeoff of zT between TE properties in bulk materials

By looking at equations (1.7), (1.8), (1.9) and (1.12) in the previous section, it is found that the Seebeck coefficient, electrical conductivity and electronic thermal conductivity are interrelated with the carrier concentration or mobility. The interdependent relationship makes the optimization of zT more complicated.

1.4.1 Effect of different carrier concentrations

To achieve a high Seebeck coefficient, two things should be guaranteed. First, there should be only one type of carrier, either electrons or holes, if there is mixing of n-type and p-type conduction, the both charge carriers which diffuse to the cold end will cancel the induced Seebeck voltage. Other than that, a material with large Seebeck coefficient should have low carrier concentration, this requirement can be expected through equation (1.7) and (1.8) mathematically. For the ease of discussion, a simplified model of Seebeck coefficient can be used. For metals or degenerate semiconductors with parabolic band and energy-independent scattering approximation, Seebeck coefficient can be written as:

$$\alpha = \frac{8\pi^2 k_B^2}{3eh^2} m^* T \left(\frac{\pi}{3n}\right)^{2/3} \tag{1.14}$$

where h in the equation is the Planck's constant. From equation (1.14), the carrier concentration is inversely proportional to the Seebeck coefficient, however by equation (1.9) and (1.12) the carrier concentration is directly proportional to the electrical conductivity and carrier thermal conductivity, so the TE material's carrier concentration should be taken under a consideration. Figure 1.6 shows a compromise between large Seebeck coefficient, high electrical conductivity and low thermal conductivity so as to maximize zT, the peak occurs when carrier concentration ranges from 10^{19} to $10^{21} cm^{-3}$, which is within the carrier concentration range of metals and heavily doped semiconductors.

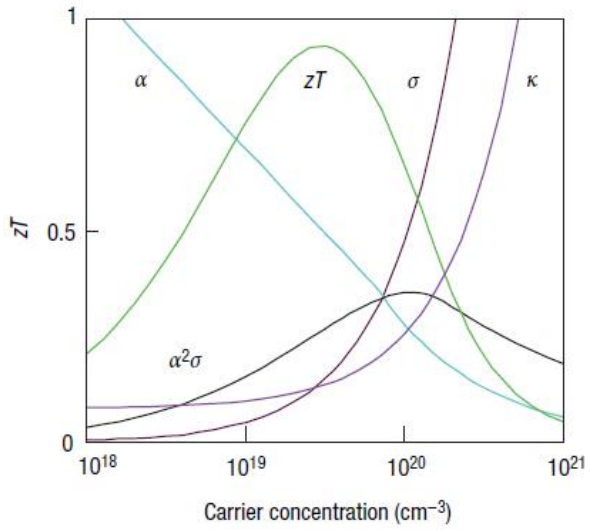

Figure 1.6. Relationship of carrier concentration to Seebeck coefficient, electrical conductivity, power factor, thermal conductivity and zT.[11]

1.4.2 Effect of different effective masses

From equation (1.14), (1.10) and (1.9), m^* refers to the density of state (DOS) effective mass. At Fermi surface of flat, narrow bands the DOS effective mass will be high. Similar to the effect of carrier concentration, a large effective mass increases Seebeck coefficient, but it will also reduce the carrier mobility, leading to a reduction of electrical conductivity and electronic thermal conductivity. So to optimize zT a compromise should be formed between high effective mass and high mobility. Among the good TE materials, materials with high mobility and low effective mass are typically made from elements with small electronegativity differences, such as SiGe and GaAs, while materials with low mobility and high effective mass usually have narrow bands, typical examples are oxides and chalcogenides.

1.4.3 Effect of thermal conductivity

The contribution of carrier in thermal conductivity is expressed in equation (1.12), in the equation the Lorenz factor varies with material's carrier concentration. In materials with low carrier concentration the Lorenz number can be reduced to 80% of the free electron value. Also the Wiedemann-Franz law does not include a bipolar term which is an uncertainty in mixed conduction, this will lead to erroneously estimation of thermal conductivity[18].

Regarding a material with low lattice thermal conductivity, glass is a good candidate.

Because of the short range order of crystal lattice in glass, the thermal conductivity in glass can be viewed as a random walk of energy rather than a rapid transport through phonons. However glass is not a good TE material because of the lack of "electron-crystal" properties. A good TE material should be a crystalline material that can scatter spectrum of phonons with wide range of mean free paths and wavelengths without making a significant disruption of electrical conductivity. Therefore a good TE material should be an unusual material with phonon scattering agents at different wavelengths.

1.5 Different approaches to enhance zT

Over the past few decades, researchers have been trying to enhance the TE figure of merit zT, and a great progress has been made. Figure 1.7 summarizes those reported zT values, where the development of thermoelectricity can be divided into three generations considering the zT values. Since the observation of Seebeck effect in 1821, zT values of different TE materials were around 1 until 1990; this was called the first generation. After Hicks *et al.*[5,6] proposed the zT enhancement by lowering materials' dimensions in 1993, the second generation of TE development has pushed the materials' zTs to about 1.7, by introducing nanostructures and size effects. Among the first and the second generation, those TE materials can be divided into three operating temperature regimes varying from $< 400\,K$ for Bi_2Te_3-based systems, $600 - 900\,K$ for PbTe-based materials and $> 900\,K$ for SiGe-based systems as shown in Figure 1.7. The third generation started from about 2010, where some new concepts

and technologies were introduced to push zT to 2.8. In the following sections, some approaches to enhance figure of merit zT will be briefly introduced.

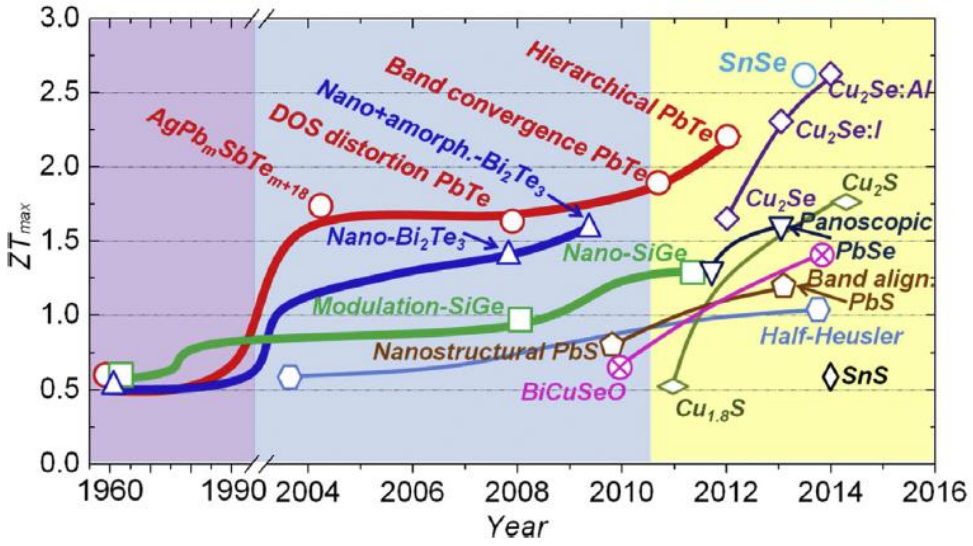

Figure 1.7. Development of TE materials in decades.[19]

1.5.1 Distortion of electronic DOS

Researchers[20,21] found that the Seebeck coefficient can be improved by doping. The basic mechanism comes from the Mahan-Sofo theory[22], which starts from the Mott expression:

$$\alpha = \frac{\pi^2}{3}\frac{k_B}{q}k_BT\left\{\frac{d[\ln(\sigma(E))]}{dE}\right\}_{E=E_F} = \frac{\pi^2}{3}\frac{k_B}{q}k_BT\left\{\frac{1}{n}\frac{dn(E)}{dE}+\frac{1}{\mu}\frac{d\mu(E)}{dE}\right\}_{E=E_F} \quad (1.15)$$

where n and μ are carrier concentration and mobility, respectively.

In this equation, the Seebeck coefficient α is energy dependent on $\sigma(E)$ taken at

Fermi energy E_F. There are two mechanisms to increase the Seebeck coefficient. The first method is to increase the energy dependence of $\mu(E)$, such as introducing a scattering mechanism that strongly depends on the energy of the charge carriers. The other mechanism is to increase the energy dependence of $n(E)$, for example by a local increase of the density of states g(E), this is the basis of Mahan-Sofo theory. In Figure 1.8a, the DOS of pure PbTe around the valence band is denoted in dashed line. If the PbTe is doped by group III elements including thallium, the DOS around dopant-related level, which is within E_R, will be increased, as illustrated as the solid line in Figure 1.8a. This phenomenon can be explained by the resonation between the valence or conduction band of the host semiconductor, and one energy level of a localized dopant atom. With the aid of DOS distortion, Heremans *et al.*[20] experimentally pushed the zT of p-type PbTe to above 1.5 by doping 2% of thallium (Tl) as shown in Figure 1.8b, which increased the electrical conductivity while maintaining the Seebeck coefficient using the distortion of DOS. Wang *et al.*[21] also demonstrated a zT enhancement of $\beta - Zn_4Sb_3$ by praseodymium (Pr) doping. These findings show a possibility on decoupling the TE properties.

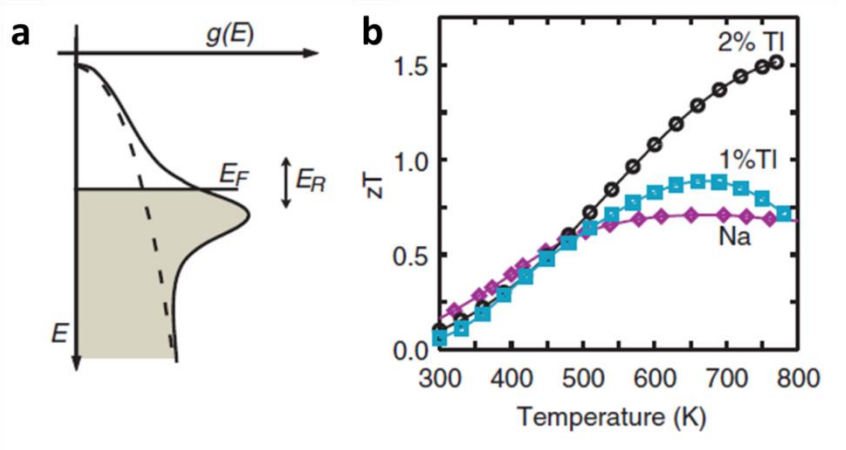

Figure 1.8. (a) Distortion of DOS in Tl-doped PbTe. (b) The *zT* enhancement of Tl-doping in PbTe.[20]

1.5.2 Low dimensional TE material

Low dimensional TE materials also show a possibility on tuning the TE properties independently. Dresselhaus *et al.*[23] suggested that when the length scale of TE material is lowered down to nanometer length scale, the electronic DOS will possibly be changed as shown in Figure 1.9, which is known as quantum confinement effect. The field of low dimensional TE started with two strategies on enhancing the TE figure of merit: (1) using quantum confinement phenomena to control and improve α and σ independently and (2) using different interfaces to filter or scatter the phonons so as to reduce thermal conductivity. Early works focused on investigating the feasibility of the mentioned concepts.

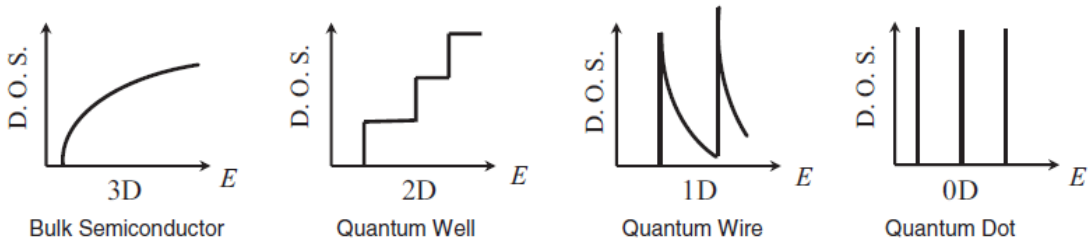

Figure 1.9. Changes of DOS in different dimensions.[23]

Hicks *et al.*[5,6] first determined theoretically the effect of low dimensional material to the *zT*, and a 2D quantum model to show the *zT* enhancement. Given an anisotropic material with one band, and with a constant relaxation time, the Seebeck coefficient α, electrical conductivity σ and electronic thermal conductivity κ_e can be presented as follows:

$$\alpha = -\frac{k_B}{e}\left(\frac{2F_1}{F_0} - \xi^*\right) \tag{1.16}$$

$$\sigma = \frac{1}{2\pi a}\left(\frac{8\pi^2 k_B T}{h^2}\right)(m_x m_y)^{\frac{1}{2}} F_0 e\mu_x \tag{1.17}$$

$$\kappa_e = \frac{\tau h^2}{8\pi^3 a}\left(\frac{8\pi^2 k_B T}{h^2}\right)^2 \left(\frac{m_y}{m_x}\right)^{\frac{1}{2}} k_B \left(3F_2 - \frac{4F_1^2}{F_0}\right) \tag{1.18}$$

where a is the width of a quantum well, m_i the effective mass components, τ the relaxation time, ξ^* and F_i are denoted as the reduced chemical potential and the Fermi-Dirac function, respectively:

$$\xi^* = \frac{(\xi - \frac{h^2}{8m_z a^2})}{k_B T} \tag{1.19}$$

$$F_i = F_i(\xi^*) = \int_0^\infty \frac{x^i dx}{e^{(x-\xi^*)} + 1} \tag{1.20}$$

Different from the corresponding parameters modeled in 3D TE materials, the TE

properties in 2D materials are related to the width of quantum well a. This means that other than the traditional tuning factors including carrier concentration and effective mass, the width of quantum well also contribute to the optimization of *zT*. The relationship between the 2D *zT* and the width of quantum well of Bismuth is simulated and constructed in Figure 1.10.

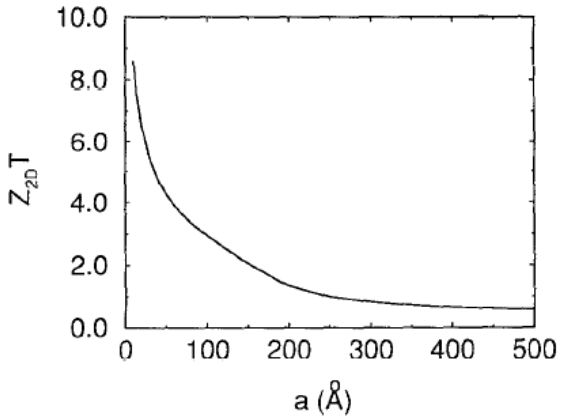

Figure 1.10. Simulation of 2D *zT* with the change of Bismuth quantum well width.[6]

The proof-of-principle that an enhanced TE performance can be obtained by low dimensional material system was first experimentally studied by Hicks *et al.*[24], by using PbTe/$Pb_{1-x}Eu_xTe$ multiple-quantum-well structures. They discovered that the n-type PbTe system can have a greater $\alpha^2 n$ when the quantum well thickness approaches 2 nm, compared to the value of the bulk PbTe as shown in Figure 1.11 where n is the carrier concentration. Not only in PbTe system, the $\alpha^2 n$ enhancement was also shown in Si/SiGe quantum well[25].

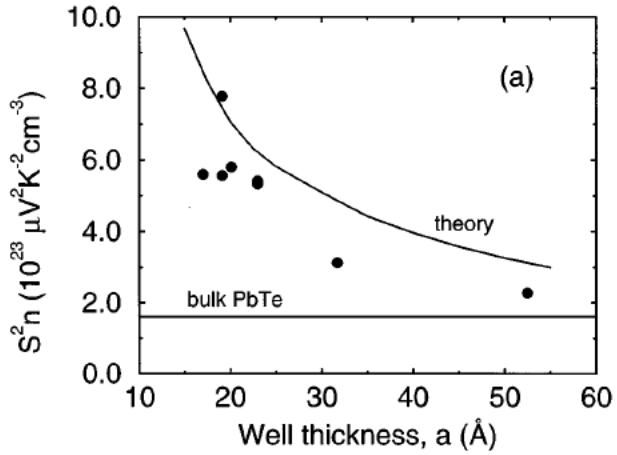

Figure 1.11. Comparison of $\alpha^2 n$ between the PbTe/$Pb_{1-x}Eu_xTe$ quantum well structure and the bulk PbTe.[24]

The proof-of-principle of the second concept mentioned above was demonstrated by Bi_2Te_3/Sb_2Te_3 superlattices[26,27], that the interfaces between the layers scatter the phonons to reduce thermal conductivity more than decreasing the electrical conductivity. Other than the superlattice structure, the reduction of thermal conductivity can also be achieved by introducing nanostructures to the material. The transport of phonon in a material carries a spectrum of wavelengths; these phonons with different mean free paths (MFP) contribute to the total thermal conductivity, and they can be scattered by different nanostructures. To be more specific, acoustic phonons with small MFP can be scattered by point defects, while phonons with medium MFP can be filtered by interfaces between precipitates and matrix in material, and grain boundaries can scatter phonons with large MFP. To scatter phonons with all wavelengths, a material should have nanostructures in all scale, which means the material should contain point defects, precipitates and grain boundaries, as illustrated

in Figure 1.12.

The strategy of all-scale hierarchical architectures were successfully demonstrated in lead chalcogenides[28-34], Figure 1.13 shows the comparison of thermoelectric performance for undoped PbTe and its nanostructured counterparts.[35] In the figure the introduction of point defects (Na) decrease the lattice thermal conductivity by ~25%, which makes the *zT* of doped PbTe increased, the enhancement can be more for further doping. These results show a quasi-independence relationship between the thermal conductivity and the electrical conductivity in low dimensional materials.

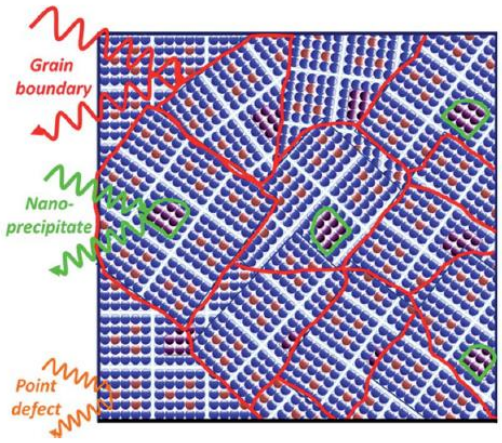

Figure 1.12. All-scale hierarchical architecture of material. It contains point defect, nano-precipitate and grain boundary corresponding in scattering phonons with short, medium and long mean free path respectively.[35]

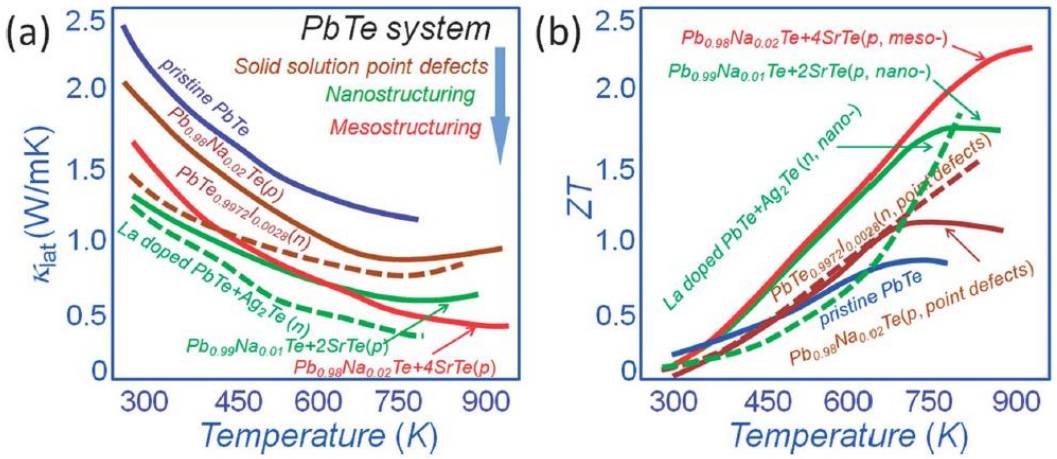

Figure 1.13. (a) Reduction of lattice thermal conductivity and (b) *zT* enhancement of PbTe by nanostructuring.[35]

1.5.3 Energy barrier scattering

TE properties of materials can also be enhanced with aid of energy barrier scattering, and typically, energy barrier scattering presents in TE materials with fine grains or nanocomposites. Given a TE material with one type of mobile carriers, when a constant thermal gradient is applied to the material, the charge carriers diffuse from the hot end to the cold end and Seebeck voltage is created. Consequently, a potential difference will be developed from the Seebeck voltage, and potential difference will drive the mobile charge carriers back to the original position and diminish the Seebeck voltage. In the whole procedure, the charge carriers undergo diffusion and drift process simultaneously. By introducing fine grains or nanocomposites, the material will have more grain boundaries, and these grain boundaries act as the potential barrier to retard the drift of carriers, therefore the Seebeck coefficient can be improved. These grain

boundaries also decrease the thermal conductivity because of the increased phonon scattering by grain boundaries.

This concept has been investigated by different researchers in theoretical and experimental ways, for bulk[36,37] and thin film scales[38,39]. Gao *et al.*[36] simulated the relationship between grain size and the Seebeck coefficient of a TE material, initially they made several assumptions for simplifying the calculation: (1) the material is homogeneous and isotropic, (2) the grains are aligned periodically, and (3) the shape of the grains are square. Using their simulation, the Seebeck coefficient of the bulk $CoSb_3$ was predicted as shown in Figure 1.14, where one can notice that the prediction agrees well with the experimental TE properties of the material[40]. Takashiri and his research group[38] also investigated the effect of grain size to the TE properties of n-type Bi_2Te_3. They deposited Bi_2Te_3 thin films with average grain sizes of 10, 27 and 60 nm, and observed that compared to the bulk material, the film annealed at 250 ℃, which was corresponding to the thin film with 60 nm grain size, showed an enhanced *zT*. Specifically, compared to the bulk material, the film annealed at 250 ℃ had an increased Seebeck coefficient, and a decreased thermal conductivity while the electrical conductivities of the thin film was in the same order of magnitude as the bulk material, notwithstanding there was a decrease. However, the other thin films with grain sizes of 10 and 27 nm did not show any improvement on *zT*, the authors explained the failure by the increase of the defect density at dirty grain boundaries, which degrades the overall TE performance. Besides the experimental work done by Takashiri and his group, Kuo *et al.*[37] and Valalaki *et al.*[39] also demonstrated enhanced *zT*s by fabricating fine-grained PbTe bulk material and reduced thickness Si thin film

respectively. In their works, they showed a reduced thermal conductivity and increased Seebeck coefficient without a significant decrease in electrical conductivity compare to the original material.

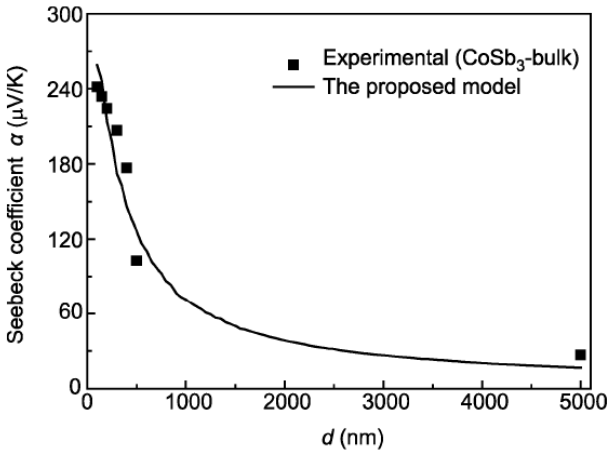

Figure 1.14. Simulation of relationship between grain size and Seebeck coefficient of $CoSb_3$ bulk material, compared with the experimental result.[36]

1.6 Motivation of this work

Compared to the study of bulk thermoelectric materials, the study of thermoelectric thin films is insufficient, especially in exploring new emerging thermoelectric materials, such as SnSe, in thin film form. For example, there is only one report by Inoue *et al.*[41] investigating the Seebeck and carrier transport of SnSe films at room temperature. There are plenty of rooms to explore new thermoelectric thin films and study approaches and mechanisms of thermoelectric property enhancement in thin film form thermoelectric materials including SnSe and SnTe thin films. This raises our

interest of enhancing TE performance of SnSe and SnTe thin films by introducing grain boundaries, or using a superlattice structure.

With increased grain boundary scattering, TE properties of SnSe and SnTe thin films are expected to be enhanced. In this work, the grain boundaries are introduced by a special deposition method called Pulsed Laser Glancing Angle Deposition (PLGLAD), which is introduced in Chapter 3.

1.7 Scope of the thesis

In chapter 2, experimental methods on thin films growth are introduced, and methods involved in structural and TE characterizations of thin films are presented. Chapter 3 presents the results and discussions of SnSe thin films and demonstrates the effect of energy barrier scattering to the TE properties. Results and discussions of SnTe films and the effect of multilayered structure to the TE properties are presented in chapter 4. Conclusions and recommendations for future work are given in chapter 5.

Chapter 2 Introduction of Experimental Methods

2.1 Thin films deposition

Thin film is a thin layer of solid material attached on a solid support called substrate. Thin films and bulk materials are different in several ways: (1) The properties of thin film are strongly influenced by the surface and interface, (2) according to the lattice mismatch and the difference in thermal characteristics between thin film and substrate, thin film may experience stress, and (3) the DOS of thin film and bulk material maybe different when the film thickness approaches quantum regime.

In depositing thin film, the thin film material experiences three steps, i.e., emission of species (atoms, ions and clusters) from the source, transport through the vacuum chamber and condensation on the substrate. The formation of thin film is schematically shown in Figure 2.1. The emitted material impinges onto the material, and they stay on the substrate surface when they lose enough kinetic energy given by the emission process. These particles adsorbed on the substrate surface are known as adatoms. At this stage the adatoms are still thermodynamically unstable and tend to desorb, and move over the surface by surface migration until they meet and interact with the other adatoms, forming a larger cluster. As the clusters are more immobile, they remain at the locations where they are formed, interact with mobile adatoms and grow into a large island. As the islands grow, different islands fuse together and form a thin film.

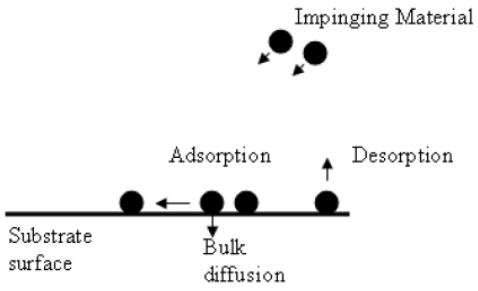

Figure 2.1. Formation of a thin film.

2.1.1Techniques of depositing thin films

Vapor deposition is commonly used in making semiconducting thin films which can be divided into two categories: (1) Physical Vapor Deposition (PVD) and (2) Chemical Vapor Deposition (CVD).

In PVD, the solid source material is vaporized and transfer to the substrate in a vacuum chamber. The pressure of the chamber should be low and that the mean free path of the source material is great enough to travel from the source to the substrate. There are several examples of PVD:

- Thermal evaporation
- Sputtering
- Pulsed laser deposition (PLD)

Thermal evaporation is one of the most widely used deposition techniques in industry because multiple wafers can be deposited simultaneously. Using thermal evaporation, the raw material is heated by the filament or boat and evaporated, the material will

then travel through the vacuum in the form of vapor and condense onto the cooler substrate to form a thin film. A vacuum chamber is needed so that the material vapor can reach the substrate without scattering by other gas atoms. Molecular Beam Epitaxy (MBE) is a complex form of thermal evaporation, but with a Knudsen effusion cell which helps directing the material vapor to the substrate.

In sputtering, the target atoms are ejected by the collision of energetic argon (Ar) ions as shown in Figure 2.2. Upon the collision, the Ar ions transfer energy and momentum to the target to liberate the target atoms. These atoms form a thin film once they condense on the substrate. Using this technique, the chamber is vented with Ar gas so as to maintain the concentration of Ar ions in the plasma. The yield of sputtering is affected by several parameters such as the concentration and energy of gas ions, target and substrate distance and strength of electric field.

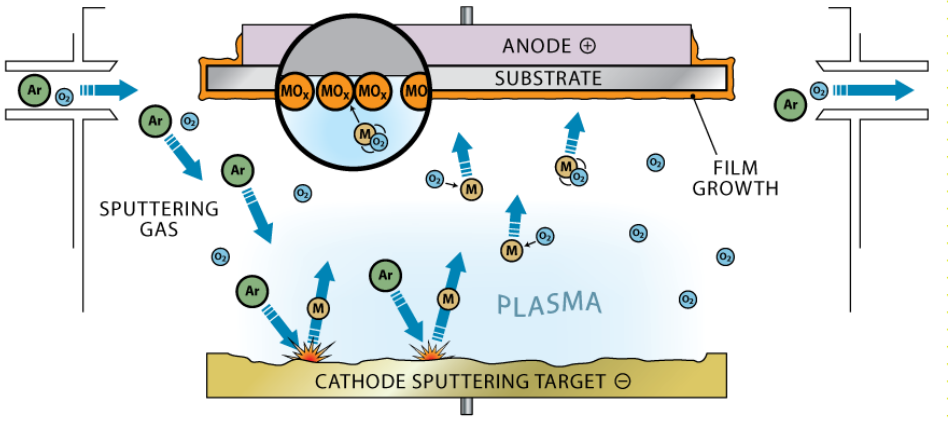

Figure 2.2. Schematic showing the process of sputtering.

The concept of PLD is represented schematically in Figure 2.3, different from thermal

evaporation and sputtering, the emission of target material is done by high energy laser. When the laser beam transmits through the quartz window and is focused onto the target by optical lens, the spot on the target exhibits superheating and the material is evaporated. The evaporated atoms will form a laser plume and condense onto the preheated substrate. Using this deposition technique, a high vacuum chamber is required so as to reduce the scattering of gas atoms. The deposition rate of PLD is strongly affected by the substrate-target distance, substrate temperature and the laser energy.

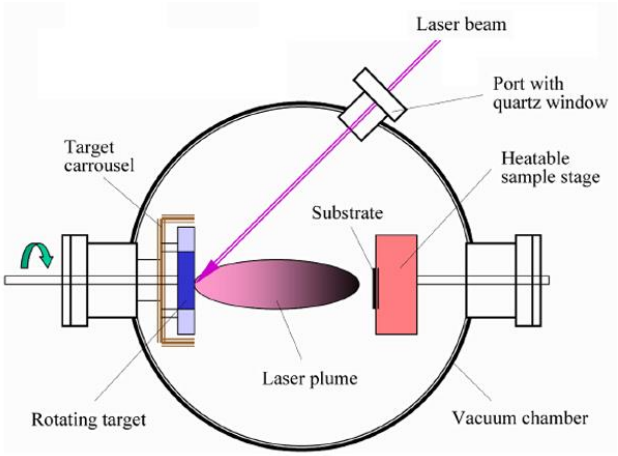

Figure 2.3. Schematic showing the setup of pulsed laser deposition.

2.2 Structural characterization of the TE thin films

After the deposition of the thin films, the crystalline phase and orientation of them were characterized by XRD (Rigaku SmartLab) with Cu K α_1 source. Then

transmission electron microscopy (TEM) (JEOL 2100F, operated at 200kV) and energy dispersive X-ray spectroscopy (EDX) study was conducted to confirm the microstructure and the composition of the films. The morphology of the as-grown films was obtained by atomic force microscope (AFM) (Asylum MFP 3D Infinity) and SEM (JEOL 6330F). The thickness of the thin films was determined by cross-sectional SEM.

2.3 Seebeck coefficient and electrical conductivity measurement

The Seebeck coefficient and electrical conductivity of the thin films were obtained by NETZSCH SBA 458 Nemesis. Figure 2.4 shows the mechanism of the measurement, where the sample is clamped onto a ceramic support and in touch with the two micro-heaters placed on both sides. Four probes are connected to the sample, with two outer probes for injecting current in the electrical conductivity measurement, and two inner probes for measuring the temperature and the voltage in the Seebeck and electrical conductivity measurement.

In the Seebeck coefficient measurement, the micro heater at one side will first apply heat to the TE material, and upon the conduction of heat in the TE material, the induced Seebeck voltage and the temperature of the two ends of the TE material are measured by the two inner probes. After a short time of temperature stabilization, the micro heater at the other end will apply heat to the TE material, so as to measure the Seebeck

voltage of the TE material in which the heat conduction in the TE material is in a reverse way. Theoretically the two measured Seebeck coefficients should be the same. After the Seebeck coefficient measurement, the electrical conductivity measurement begins once the temperature between the two ends of TE material is in equilibrium. A dc current is injected into the TE material through the two outer current pins, and at the same time the voltage pins measure the potential difference between the middle two ends of the material.

In measuring the Seebeck coefficient, there is no difference between thin film and bulk material. However, the derivation of equation between the film and bulk material is different in measuring electrical conductivity.

Figure 2.5 shows the electrical potential of the thin film in point shape four-point collinear probe method. Given that the electrodes are point shape, the film's width is larger than the diameters of electrodes, the equipotential lines, denoted as dotted lines, are cylindrical shape. Also, the shape of the equipotential line will change with respect to the travel distance from the probe. The resistance between two equipotential lines can be expressed as:

$$\mathrm{dR} = \frac{\rho}{2\pi r d} dr \tag{2.1}$$

where ρ is resistivity of the material, r is the distance between the two lines and d is the film thickness. Assume the distance between probe 1 and 2, probe 2 and 3 and probe 3 and 4 are S_{12}, S_{23} and S_{34} respectively, the potential difference across the two inner probes, probe 2 and 3, can be expressed as:

$$V_{23} = \frac{\rho I}{2\pi d} ln[\left(\frac{S_{34}+S_{23}}{S_{12}}\right)\left(\frac{S_{12}+S_{23}}{S_{34}}\right)] \tag{2.2}$$

where I is the input current. In this work, the films used in the electrical conductivity

measurement has been deposited a layer of gold (Au) electrode, as shown in Figure 2.6, the Au electrode protects the film and promotes the conduction between the film and the probe. In addition, the equipotential line maintains its shape throughout the travel, which is the same as the bulk material measurement, so the electrical conductivity calculation of thin films in this work can be treated as that of the bulk material.

In bulk material, the electrical conductivity can be calculated by $\sigma = \frac{Ix}{Vwt}$, where σ is electrical conductivity, I is injected current, x is the separation between the two voltage pins, V is measured voltage, w is width of sample and t is the thickness of sample.

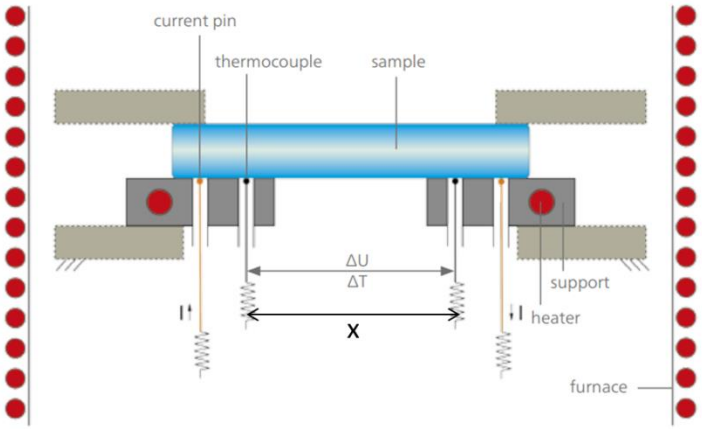

Figure 2.4. Experimental setup in measuring Seebeck coefficient and electrical conductivity.

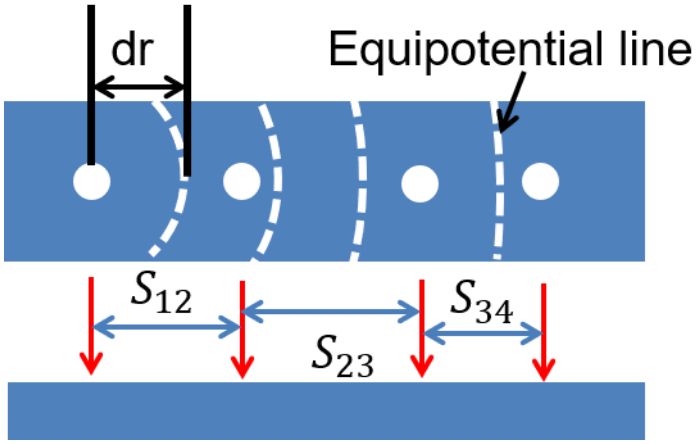

Figure 2.5. Schematics showing the electrical potential on thin film in point shape four-point collinear probe method, in in-plane view and cross-sectional view.

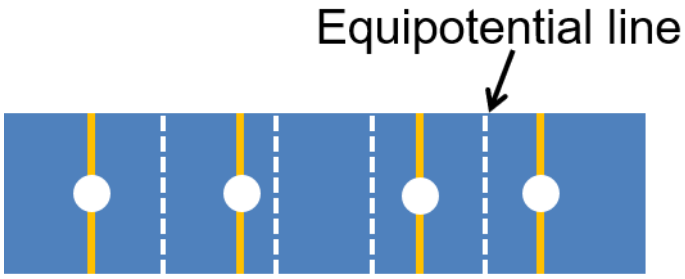

Figure 2.6. Schematics showing the electrical potential on thin film in line shape four-point collinear probe method.

2.4 Thermal conductivity measurement

In this work, the thermal conductivities of the thin films are measured by well accepted 3ω method[42]. At the very beginning, 3ω method was used for measuring the thermal diffusivity of incandescent light bulb filaments[43], so as to investigate the lifetimes of

metal filament and carbon filament[44]. Later 3ω method was applied in measuring thermal diffusivity of liquids[45] and dielectric solids[46]. The first application on measuring solid thermal conductivity by 3ω method was reported by Cahill *et al.*[47] at 1987.

When using the 3ω method, the surface of thin film should be insulating. In this work, since SnSe, SnTe and the multilayered film composed by them are semiconducting, a layer of Al_2O_3 was first deposited by ALD on the films and a bare substrate serving as a reference sample. This Al_2O_3 layer is electrical insulating which prevents current leakage during the measurement. In this work, the thickness of the insulating layer is 160 nm. After the deposition of insulating layer, a patterned metal thin film with known dimension was deposited on the samples, as shown in Figure 2.7. Cr/Pt was used as the metal line with the dimension of length 1000 μm, width 20 μm and thickness 110 nm. The metal thin film was used as a heater and a thermometer.

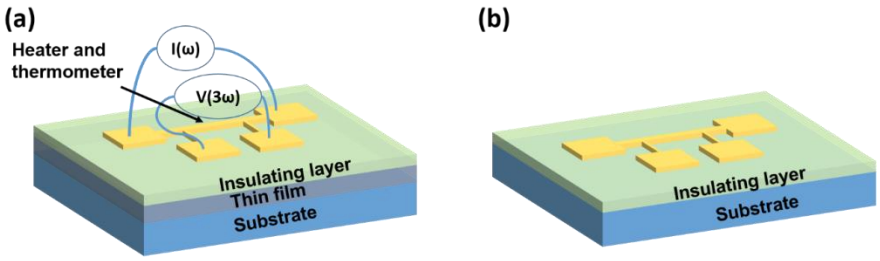

Figure 2.7. Schematics of 3ω measurement in measuring (a) thin film and (b) reference sample.

During the measurement, an AC current was applied to the outer pads of the metal line, the current can be expressed by:

$$I = I_0 sin\omega t \tag{2.3}$$

where I_0 is the current amplitude, ω is the angular frequency of the current signal. The injection of current causes joule heating of the metal, the power of the joule heating can be represented by:

$$P = I^2 R$$

$$P = \frac{I_0^2 R}{2} - \frac{I_0^2 R}{2} cos2\omega t \tag{2.4}$$

where R is resistance. The induced joule heating leads to the temperature oscillation of the heater:

$$\Delta T = T_{DC} + T_{AC} \cos(2\omega t + \phi) \tag{2.5}$$

In equation (2.5), the temperature oscillation of the heater is directly proportional to the joule heating, with a phase lag term ϕ, T_{DC} and T_{AC} are denoted as the constant term and time-dependent term of temperature in which they are related to the first and second term in equation (2.4), respectively. The resistance of metal line varies with the temperature, it can be given by:

$$R = R_0(1 + \alpha \Delta T) \tag{2.6}$$

where R_0 is the resistance in reference temperature, which is room temperature, and α is the temperature coefficient of resistance (TCR). By substituting equation (2.5) into equation (2.6), the following expression of resistance can be obtained:

$$\mathrm{R} = R_0[1 + \alpha T_{DC} + \alpha T_{AC} \cos(2\omega t + \phi)] \tag{2.7}$$

The potential difference as the current passes through the metal line is measured:

$$\mathrm{V} = \mathrm{IR} = I_0 sin\omega t \times R_0[1 + \alpha T_{DC} + \alpha T_{AC} \cos(2\omega t + \phi)$$

$$= I_0 R_0[(1 + \alpha T_{DC}) sin\omega t + \frac{\alpha T_{AC}}{2} \sin(3\omega t + \phi) - \frac{\alpha T_{AC}}{2} \sin(\omega t + \phi)] \tag{2.8}$$

In equation (2.8), there are three sine functions, the first function does not contain

information of the time-dependent temperature term, T_{AC}. The last function contains T_{AC} term, but it carries the same angular frequency as the first term, which cannot be decoupled from the first term. And the middle term has an angular frequency of 3ω while carrying the information of T_{AC}, so analysis will be done on this term. A lock-in amplifier is used to filter out the signals with frequency of ω, and amplify the remaining voltage signal with angular frequency of 3ω. As mainly the signal with 3ω frequency is measured and analyzed, the method is called 3ω method.

The amplitude of the acquired signal, namely $V_{3\omega}$, carries information of T_{AC}, and it can be expressed as:

$$V_{3\omega} = \frac{1}{2}\alpha T_{AC} I_0 R_0 \tag{2.7}$$

In addition, $V_{3\omega}$ is a function of the frequency of the signal f. So in the 3ω measurement, the amplitude of $V_{3\omega}$ is measured at a constant temperature, with changing frequencies. The results can be fitted with a linear equation:

$$V_{3\omega} = \mathrm{S}\ln(2\pi f) + c \tag{2.8}$$

Where S is the slope in relationship of $V_{3\omega}$ vs $\ln(2\pi f)$. And from equation (2.8) and (2.7), the expression between T_{AC} and $\ln(2\pi f)$ can also be obtained:

$$T_{AC} = \mathrm{S}'\ln(2\pi f) + c' \tag{2.9}$$

Here T_{AC} is the time-dependent temperature of the total structure, which is an addition of substrate time-dependent temperature $T_{AC}^{sub.}$ and film time-dependent temperature T_{AC}^{film}. To obtain T_{AC}^{film}, T_{AC} should be subtracted by $T_{AC}^{sub.}$, which can be obtained from a similar measurement on the reference sample.

T_{AC}^{film} relates to the film thermal conductivity κ^{film} directly. Similar to the electrical conductivity, thermal conductivity is the rate of heat transport per unit area to the

change of temperature, it has a general expression as shown in the following:

$$\kappa^{film} = \frac{\mathrm{Pd}}{AT_{AC}^{film}} \tag{2.7}$$

where κ^{film} is the thermal conductivity, P is the rate of heat transport $\frac{dQ}{dt}$, which is the input power in short, d and A are the length and the cross-sectional area of the material where heat transfers. The substitution of the dimension parameters depend on the direction of heat flow in the measurement, Bogner *et al.*[48] demonstrated 3ω measurement on AlN thin film, in cross-plane and in-plane direction. They concluded that the direction of heat flow is governed by the width of the metal line, as shown in Figure 2.8, so if the metal line width is greatly larger than the film thickness, the heat flow will mainly be in cross-plane direction. Reversely, when the thickness of film is much larger than the width of metal line, the sensitivity of the thermal conductivity measurement in in-plane direction will be increased.

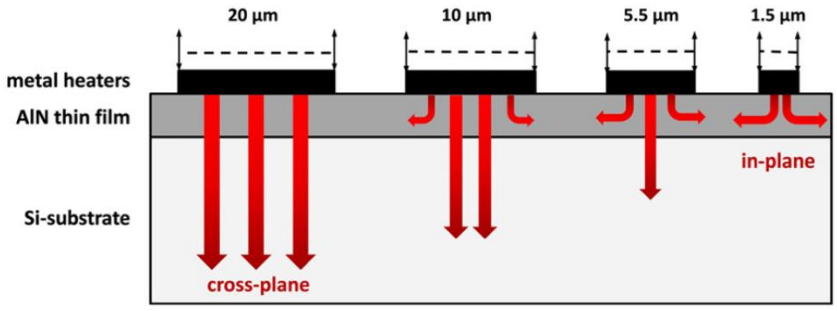

Figure 2.8. Cross-sectional schematic showing the heat flow direction with respect to the metal line width. When the metal line width is much smaller than the film thickness, the sensitivity of the thermal conductivity measurement in in-plane direction increases.[48]

The thin film thermal conductivity measured by 3ω method is precise, because in the measurement, a reference sample is used to eliminate all the thermal conductivity contribution except the studied film. Also because of the small surface area of the metallic line, the temperature stabilizing time can be reduced down to several minutes, and the effect of black body radiation can be reduced.

Chapter 3 Enhanced thermoelectric properties of SnSe thin films grown by Pulsed Laser Glancing-Angle Deposition

3.1 Introduction

Tin Selenide (SnSe) is a semiconductor adopts a simple layered orthorhombic crystal structure as shown in Figure 3.1, with lattice parameters of a = 1.149 nm, b = 0.444 nm and c = 0.4135 nm. Along the b-c plane, there are two-atom-thick SnSe slabs. Within the plane of slabs the SnSe bond is strong, while along the a-axis the layers of slabs are linked by weak bond. The structure of SnSe contains highly distorted $SnSe^{7}$ coordination polyhedra, with four long and three short Sn-Se bonds. Upon heating, the lattice parameters along b- and c-axes approach each other whereas that along a direction increases continuously; until the temperature reached 807 K, the low symmetry SnSe phase of *Pnma* (#62) space group will have a second order displacive transformation to the high symmetry phase (space *Cmcm*, #63)[49], the lattice will then expand by 2.5%.

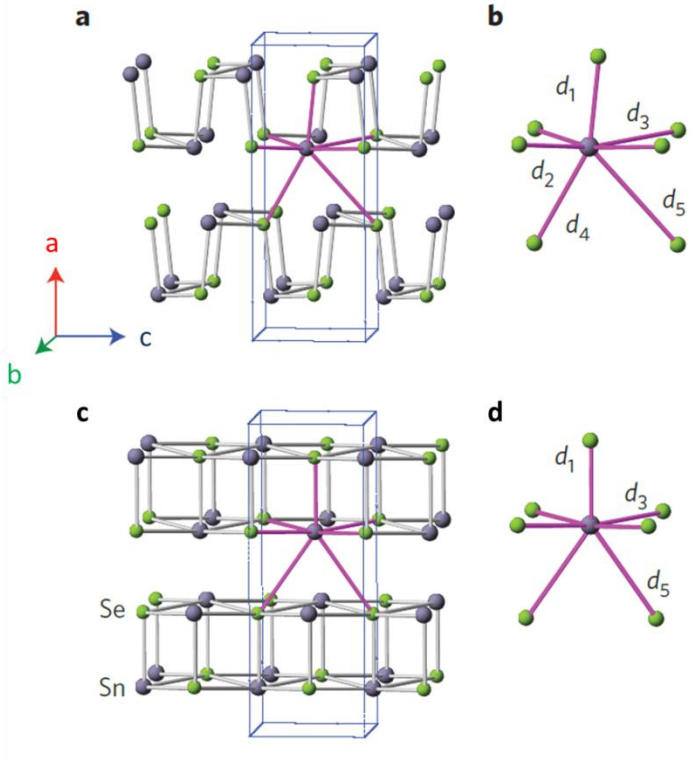

Figure 3.1. Crystal structure of SnSe in (a) *Pnma* and (c) *Cmcm* phase. (b), (d) Sn coordination polyhedron corresponding to (a) and (c) phase respectively. Sn atom is surrounded by 7 Se atoms.[50]

SnSe also has an energy gap of 0.86 eV, a hole concentration in range of 10^{17} – 10^{18} cm^{-3}, a room temperature electrical resistivity about 10^{1} – 10^{5} Ωcm^{-1} and a large optical absorption coefficient[51]. Because of the large electrical resistivity and optical absorption coefficient, it was ignored as a candidate of TE material and researchers were more interested in the optical and optoelectronic properties of SnSe[52-58]. Recently, researchers discovered that SnSe has remarkable TE properties, exhibiting the ultralow thermal conductivity[59], and this low thermal conductivity is surprising for a single crystal material.

The reason for SnSe attaining low thermal conductivity can be explained by the anharmonicity of the Sn-Se bonds in different directions[51]. The concept of harmonicity can be explained by using Figure 3.2, assuming there is a harmonic bond, when phonon travels along the bond, the potential energy experienced by an atom is proportional to its displacement from the equilibrium position, by a factor called spring constant. For the anharmonic case, the spring constant varies with the atom displacement, so that when the first phonon passes through the bond, it will change the spring constant of the second phonon, in such case the continuous phonons can be effectively scattered.

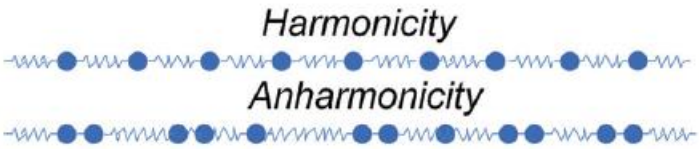

Figure 3.2. Schematic representation of harmonicity and anharmonicity.[51]

In the basis of atomic level, the anharmonic bonding of SnSe is realized in the wide range of bond lengths between Sn and Se atoms. From Figure 3.1b, it can be seen that in the $SnSe^{7}$ coordination polyhedron, a Sn^{2+} atom is surrounded by 7 Se atoms with different bonding lengths; and according to the bonding lengths they have a mix of weak, medium and strong interactions, leading to the anharmonicity of SnSe single crystals. Other than the wide range of bond lengths, the geometry of bonding also contributes to the anharmonicity of SnSe. As shown in Figure 3.1a, along the *b*-*c* plane the slabs have a zig-zag accordion-like geometry, so when the slabs are mechanically stressed, instead of changing the bonding length, the slabs will be deformed like an elastic spring. In *a* direction the weak bonding between the slabs acts as a cushion

when stress is applied.

The anharmonicity of SnSe can be determined by Grüneisen parameter, the higher the parameter, the anharmonicity will be stronger. The average Grüneisen parameters of SnSe along *a*, *b* and *c* axes are 4.1, 2.1 and 2.3, respectively[51]. Compared to Lead Telluride (PbTe), which has good physical and chemical properties as a candidate of TE material, and with the Grüneisen parameter of 1.45, the parameters of SnSe along the three directions are still higher, indicating the anharmonicity of SnSe.

In terms of power factor, compared to the other state-of-the-art TE materials, SnSe has a low power factor at room temperature and a moderate power factor at high temperature. However these results do not hinder the investigation of SnSe in the field of TE, because SnSe has a very low thermal conductivity. Researchers can therefore mainly focus on improving its power factor[60].

Nevertheless, in contrast to the considerable progress of bulk SnSe in TE field[59-63], there were relatively less studies on thin film SnSe. This is one of the motivations for us to study the growth and TE properties of SnSe thin films.

3.2 Film Deposition

The objectives of this chapter are to investigate the growth of SnSe thin films with different parameters, such as deposition temperatures and substrates, and demonstrate the grain size effect to the TE properties. The SnSe thin films were deposited on different substrates using PLD, at different temperatures of 250, 310, 330 and 350 ℃. Finally the TE properties of them including the in-plane Seebeck coefficient, in-plane

electrical conductivity and out-of-plane thermal conductivity were characterized.

The grain size of the thin films can be reduced by two methods: (1) By depositing the films at a lower substrate temperature and (2) by depositing the films at a glancing angle.

The fact that grain size in thin film can be reduced by lowering the substrate temperature has been proved by different group of researchers. Acosta *et al.*[64] discovered that the grain size increases with the substrate temperature. By plotting the relationship between the grain size and substrate temperature, Bilgin *et al.*[65] obtained a concave down curve suggesting that the grain size increased and reached a constant when the substrate temperature approached certain value. Ashour[66] and Patil *et al.*[67] obtained a curve which is concave upwards, indicating that the grain size keep increases.

Glancing angle deposition of thin films has been demonstrated to be able to control the grain size of the films[68-70], it can only be used in deposition techniques with directionality between the source material and substrate. In the deposition process, the surface of substrate is nearly perpendicular to the target, and that the small angle of adatoms to the substrate causes a shadowing effect as shown in Figure 3.3. After adatoms form immobile clusters, the clusters stop the source flux from entering the region right behind them. When the clusters keep growing, they stop the merging of grains, finally the thin film forms a structure of nanopillar array inclined towards the target.

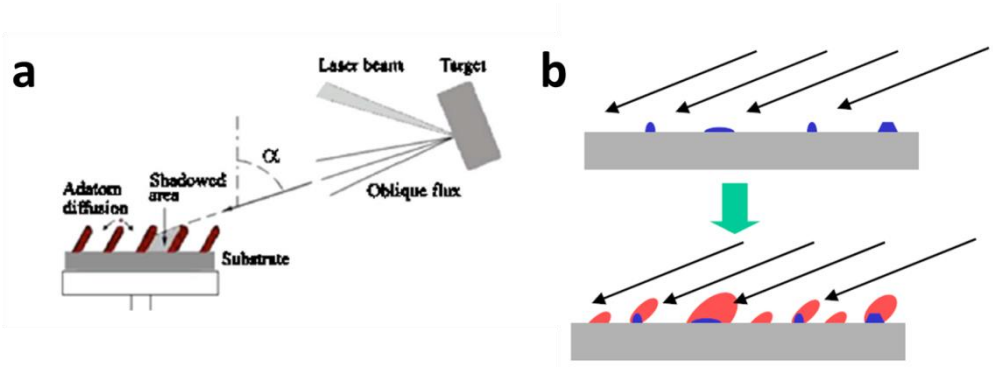

Figure 3.3. (a) Setup of glancing angle deposition. (b) Growth of thin film in glancing angle deposition.

In deciding how to fabricate the thin films, it is better to determine the method of reducing grain size first because the two mentioned methods limit the choice of deposition techniques, for example, the method of glancing angle deposition can only be used in some deposition techniques that the source flux is directional to the substrate. Considering the method of lowering the substrate temperature in reducing grain size, it should be noticed that the substrate temperature does not only influence the grain size, but also the crystallinity of the thin film. When the substrate temperature decreases continuously, it can be foreseen that the thin film will have grain size reduction, and the material will change from crystalline to amorphous material gradually, and that the TE thin films may lose their outstanding properties as crystalline such as the low thermal conductivity for SnSe and high electrical conductivity for SnTe. In contrast, without changing the substrate temperature, only the change of angle (α in Figure 3.3a) between the normal of target and normal of substrate is required for the glancing angle deposition, this ensures the crystallinity of the thin films. So in reducing the grain size of the thin film, the method of glancing angle deposition is chosen.

In applying glancing angle deposition into the as-described deposition techniques, the directionality between substrate and target should be taken in consideration. Among the aforementioned deposition techniques, only the substrates deposited by PLD and CVD are directional to the source flux, so the consideration is made between them. In this work PLD is chosen in depositing the thin films, because PLD has several advantages over CVD as described in the followings. For CVD although there are sufficient studies growing $SnSe_x$ thin films, many of them require the use of specialized precursor materials or catalysts[71,72], this is a challenge in using CVD that it requires thorough understanding of chemical reactions between the precursors. In contrast, the reaction in PLD is simple as it only requires the target which is the same as the thin film, and PLD is designed for growing the chalcogenide films[73-75] including SnSe and SnTe, so in this work PLD is more favorable in depositing SnSe and SnTe films. The laser source used in this work is KrF excimer laser, with a wavelength of 248 nm and repetition rate of 10 Hz, the substrate and target distance is 30 mm, the deposition time and substrate temperature will be discussed in the later sections with aid of the cross-sectional Scanning electron microscopy (SEM) image analysis and X-ray diffraction (XRD) analysis.

In choosing a suitable substrate for TE measurements, it should be noticed that the electrical contribution of substrate in the TE measurement should be prohibited, as in Seebeck and electrical conductivity measurement, the contribution of the substrate can greatly affect and cause errors to the obtained result. In other words, the chosen substrate should be electrically insulating, at least between the film and the substrate. In this work, silicon (Si) substrate with 300 nm of SiO_2 top layer was used, where the

SiO_2 layer served as electrical insulation between the Si substrate and the thin films. In addition, the amorphous top layer promoted the growth of polycrystalline thin film, given the goal in this work is to reduce the grain size of the thin film. To observe the growth of SnSe film, Sodium Chloride (NaCl) substrate was also chosen to deposit the film.

3.3 Structural characterization of SnSe films deposited at normal angle and glancing angle

XRD study was carried out on the SnSe films deposited on Si substrate with a 300 nm thick SiO_2 top layer, at 250, 310, 330 and 350 ℃. Figure 3.4 shows the XRD patterns of these samples, where the peaks at 2θ = 15.4 °, 31.1 ° and 64.8 ° correspond to the (200), (400) and (800) diffraction peaks of orthorhombic SnSe (a = 1.149 nm, b = 0.4153 nm, and c = 0.444 nm, JCPDS #48-1224), respectively. This implies that the SnSe films are preferentially grown along *a*-axis, being consistent with the layered structure characteristic of SnSe along *a*-axis.

In a detailed analysis, the XRD patterns show that there are (200), (400) and (800) planes for all of the SnSe films deposited at different temperatures, while the (200) and (800) diffraction peaks significantly decrease when the deposition temperature reached 350 ℃. Besides those mentioned preferential peaks, there are presences of additional peaks (302) and (122) planes in the SnSe film grown at low temperature of 250 ℃. It is obvious that the intensities of these peaks reduce when the deposition temperature reached 310 ℃, and the (302) and (122) planes vanish when the deposition temperature

reached 350 ℃. Furthermore, the additional peaks (201), (311) and (511) planes present at higher deposition temperatures (330 ℃ and 350 ℃). Based on this detailed XRD analysis, it can be concluded that 330 ℃ is close to the optimized deposition temperature of SnSe thin film.

In order to compare the morphologies of the original SnSe film and the film deposited at a glancing angle, the AFM and SEM studies of the SnSe film deposited at a normal angle will be discussed in the later section.

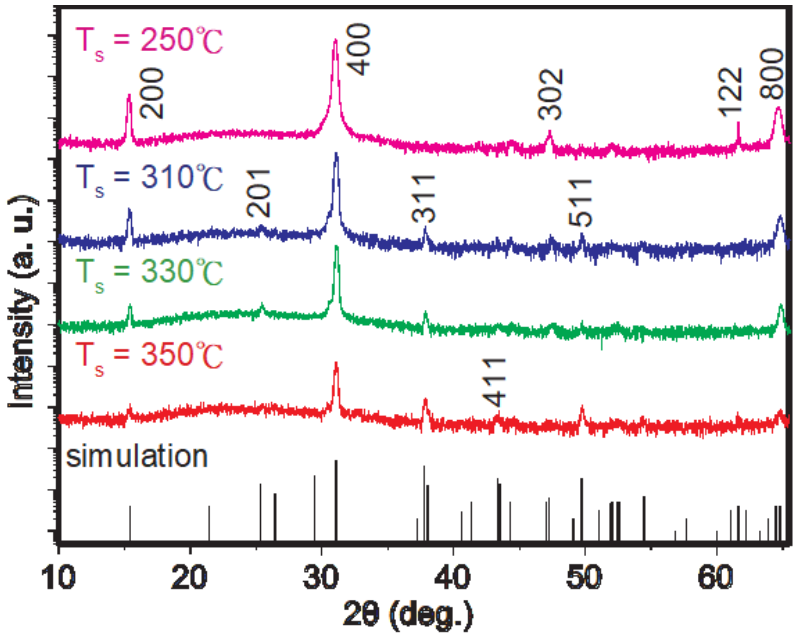

Figure 3.4. XRD patterns of the SnSe thin film deposited at a normal angle and the substrate temperatures of T_s = 250 ℃, 310 ℃, 330 ℃, 350 ℃. The patterns are compared to the SnSe simulation pattern (JCPDS #48-1224).

The microstructure and chemical composition of the as-grown thin films were investigated by TEM and EDX analysis. Figure 3.5 is a typical high-resolution TEM image (HRTEM) of the SnSe thin film deposited at 330 ℃. It shows different grains of

the as-deposited film. A Selected Area Electron Diffraction (SAED) pattern is shown in Figure 3.6, where the diffraction rings indicate that the SnSe film has a polycrystalline structure. Moreover from Figure 3.6, (111), (311) and (122) planes, with d-spacing of 3.44, 4.24 and 6.68 nm, can be indexed respectively. These results match some of the peaks obtained from the XRD pattern. Figure 3.7a shows a HRTEM image of the SnSe thin film at a selected area. In the figure, the analyzed lattice plane distances and angles between those lattice planes indicate an orthorhombic SnSe (a = 1.149 nm, b = 0.4153 nm, c = 0.444 nm) thin film, which is consistent with the aforementioned XRD results. The composition of Sn and Se is indicated by the EDX pattern shown in Figure 3.7b (noted that the Cu peak belongs to the copper grid), in the quantitative EDX analysis, the ratio of composition of Sn and Se is around 1:1, suggesting the formation of SnSe compound.

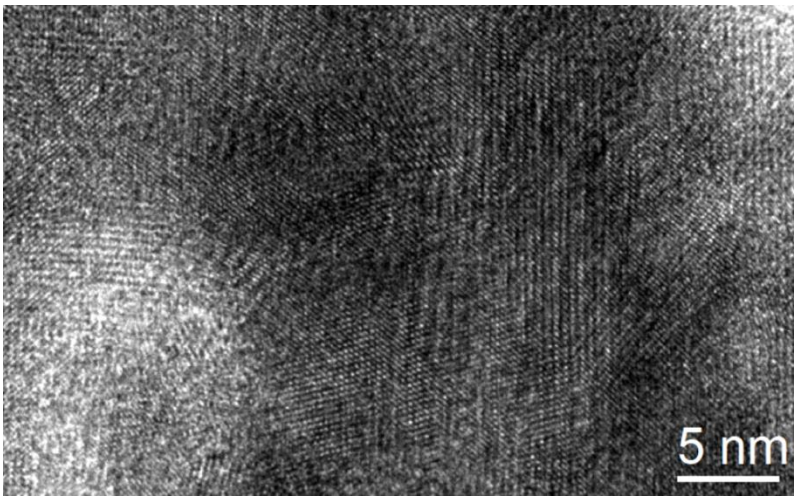

Figure 3.5. HRTEM image showing the polycrystalline structure of the as-deposited film.

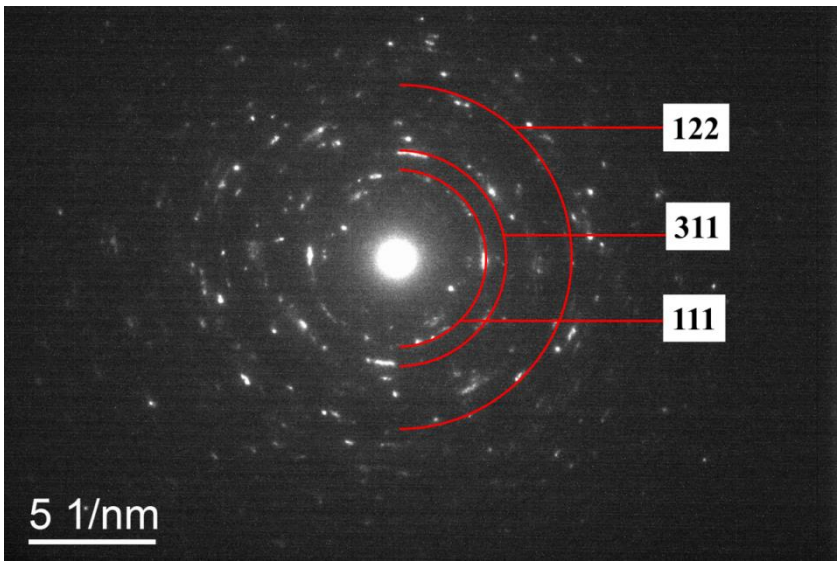

Figure 3.6. Diffraction pattern of the area in Figure 3.5.

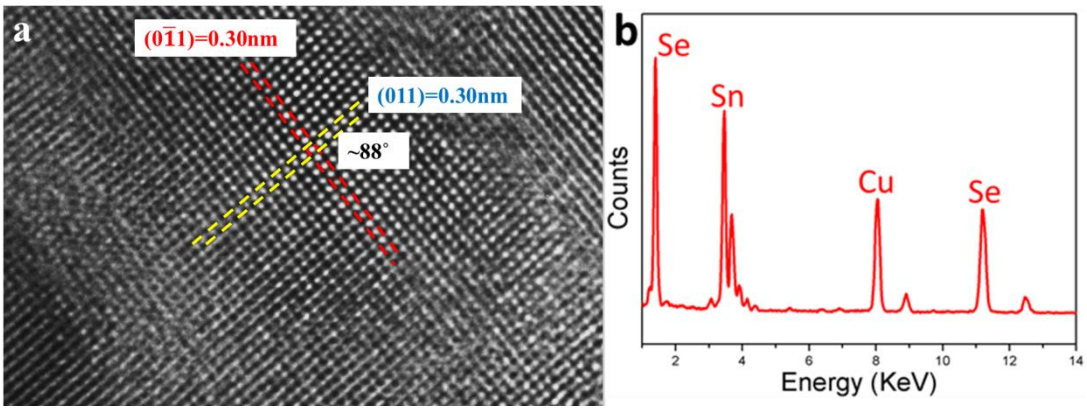

Figure 3.7. (a) HRTEM image showing (011) and (0$\bar{1}$1) planes with 88 ° between the planes and (b) EDX spectrum of SnSe thin film deposited at a normal angle with T_s = 330 ℃.

Additional thin films were deposited on NaCl at 330 ℃, in order to investigate the epitaxial growth of SnSe. The epitaxial SnSe thin film has been realized by Inoue *et al.*[41]. They analyzed the relationship between the lattice parameters of SnSe and NaCl

in different axis, and discovered that when the lattice of SnSe has an angle of 45 ° with the lattice of cubic NaCl, as shown in Figure 3.8, the lattice mismatch between SnSe and NaCl can be reduced to -3.9% for *b*-axis, and -10% for *c*-axis, which is favorable for epitaxial growth of SnSe film.

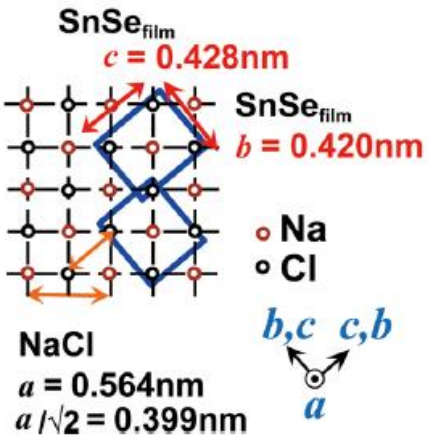

Figure 3.8. In-plane epitaxial relationship between NaCl (100) and SnSe thin film.[41]

The epitaxial SnSe films in this work were deposited at a laser repetition rate of 1 Hz, with different deposition times of 5 and 10 minutes. An XRD analysis had been conducted on these samples, and the XRD patterns are illustrated in Figure 3.9. Among all these SnSe films, they show the (200) and (400) diffraction peaks of NaCl, which are located at 2θ = 31.75 ° and 66.33 ° respectively. By observing the film with 5 minutes deposition time, the XRD pattern indicates the (400) peak of orthorhombic SnSe (a = 1.149 nm, b = 0.4153 nm, c = 0.444 nm, JCPDS #48-1224), at 31.04 °. When the film is grown for up to 10 minutes, addition diffraction peaks of (200) at 2θ = 15.45 ° and (800) at 2θ = 64.87 ° are developed. Similar to the XRD pattern of SnSe

film on SiO_2/Si substrate, these three diffraction peaks are planes along *a*-axis, which indicates a preferential growth of SnSe film on NaCl substrate.

Additionally, besides those preferential orientations, a (302) peak appears in the thicker sample. This result suggests that when the film grows thicker, there will be strain relaxation, such that point defects and dislocations will be introduced, leading to defects in the lattice and decreased quality of the single crystal film.

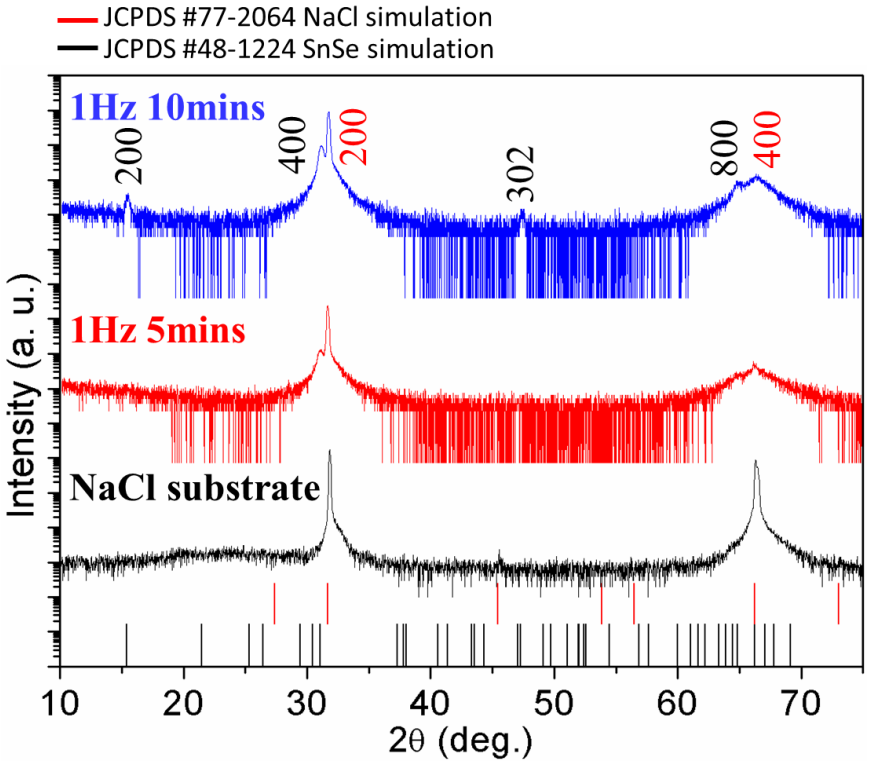

Figure 3.9. XRD patterns of SnSe films deposited on NaCl, with a comparison of bare NaCl substrate, NaCl simulation (JCPDS #77-2064) and SnSe simulation (JCPDS #48-1224).

The SnSe sample with 5 minutes deposition time has been used to investigate the

microstructure by using TEM. To prepare the TEM sample, the as-deposited film was put into water carefully, with the film facing up. After the substrate dissolved and detached from the film, a copper mesh grid with carbon film was used to obtain the floating SnSe film. Figure 3.10a illustrates the TEM image of the sample, where it can be seen that there is NaCl residue marked by circles. SAED analysis was carried out in the area enclosed by the rectangle, where it is apparent that there is NaCl residue, its diffraction pattern can also be shown in Figure 3.10b. With the aid of notation, it is observed that the diffraction pattern shows the (011), $(0\bar{1}1)$ and (002) plane of SnSe, together with (022) plane of NaCl, this reflects the epitaxial relationship of SnSe and NaCl. A region without NaCl residue is selected to investigate the single crystal SnSe only.

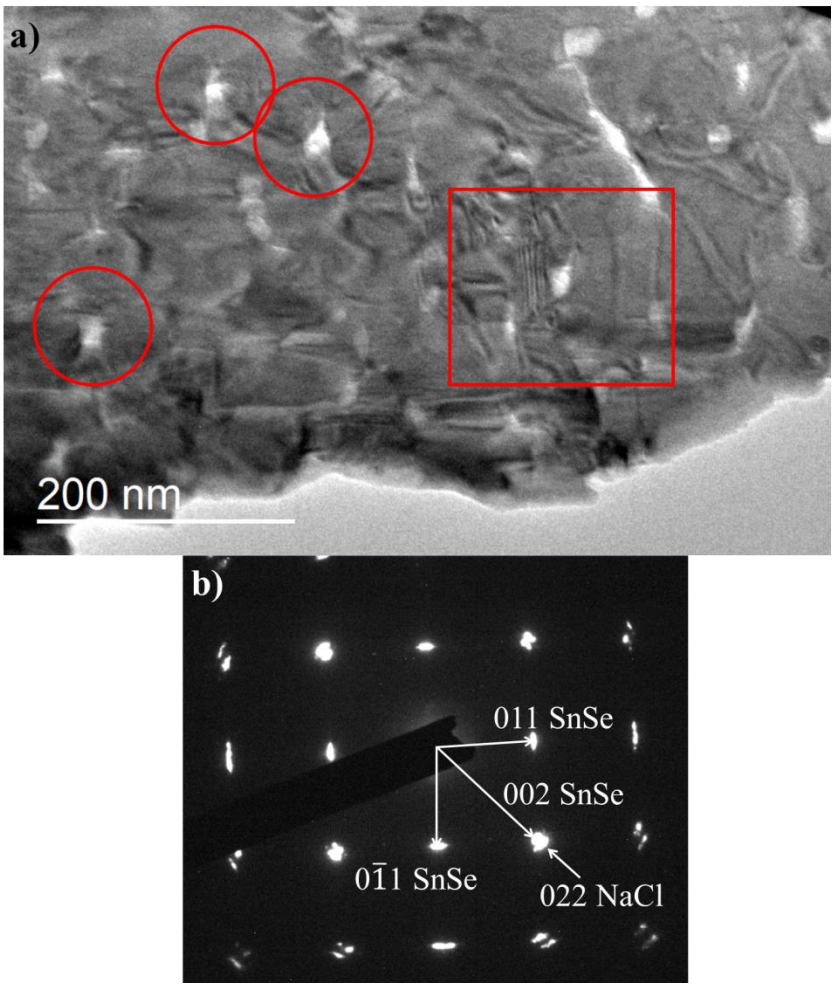

Figure 3.10. (a) TEM image of SnSe thin film deposited on NaCl at 1 Hz laser repetition rate, 5 minutes deposition time and 330 ℃. The rectangle denotes the area where the SAED is conducted. The circles show the residue of NaCl during dissolving the substrate. (b) Diffraction pattern at the area enclosed by the rectangle.

The HRTEM image of the selected area is shown in Figure 3.11. It can be seen that the SnSe film is single crystal-like, indicating that the quality of the SnSe film is very good. The analyzed image shows the (011) and (0$\bar{1}$1) planes of orthorhombic SnSe (a = 1.149 nm, b = 0.4153 nm, c = 0.444 nm) thin film, in which they both have an interplanar

distance of 0.3 nm, and the angle between these two planes is 89 °. Figure 3.12 illustrates the diffraction pattern of the SnSe film in the area of Figure 3.11, the analyzed diffraction pattern shows the (011), $(0\bar{1}1)$ and (002) planes of the single crystal SnSe.

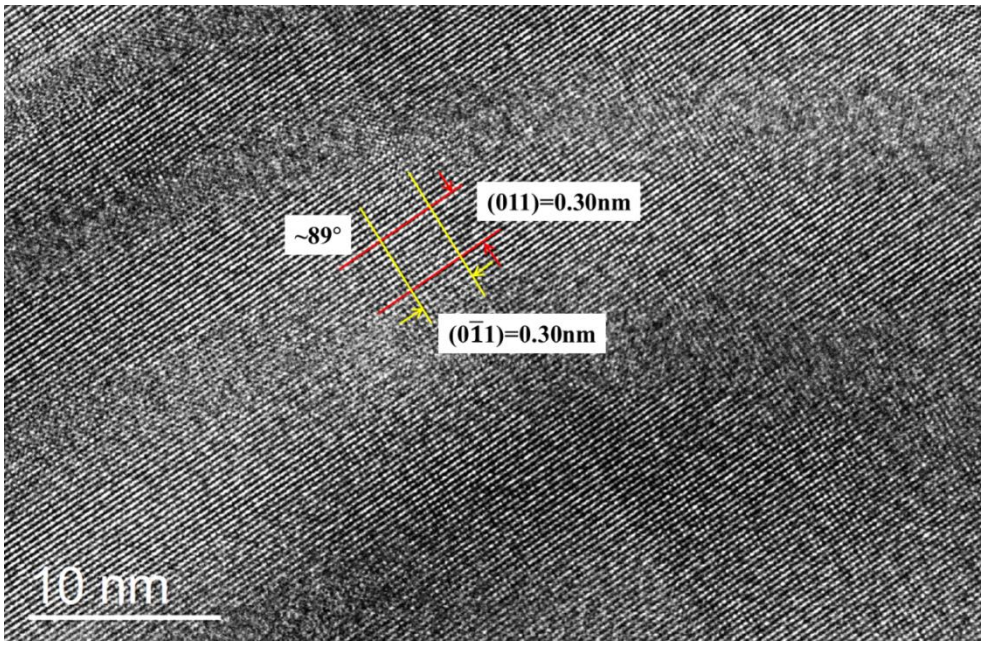

Figure 3.11. HRTEM image of SnSe thin film deposited on NaCl at 1 Hz laser repetition rate, 5 minutes deposition time and 330 ℃, showing (011) and $(0\bar{1}1)$ planes with 89 ° interplanar angle.

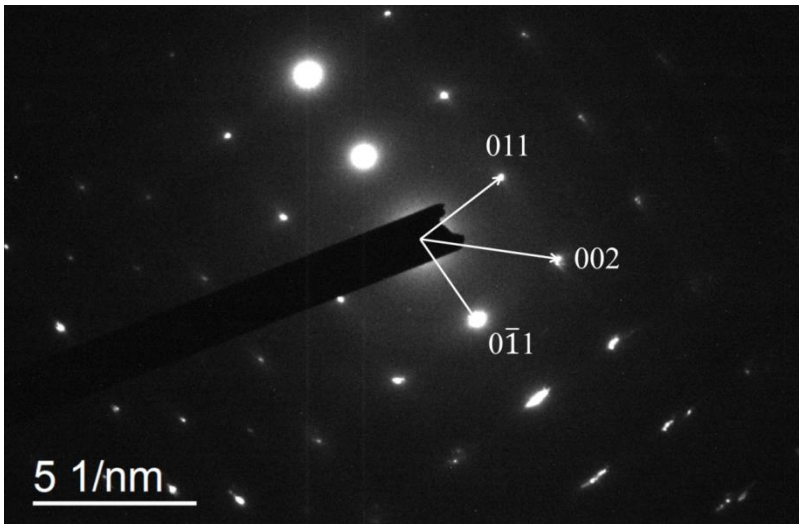

Figure 3.12. Diffraction pattern of the area in Figure 3.11.

The alternative SnSe thin film was deposited on silicon substrate with a layer of 300 nm SiO_2, at 330 ℃ and an 80 ° glancing angle, to study the effect of glancing angle deposition on the morphology and the grain size. Figure 3.13 shows its XRD pattern as a comparison with the SnSe film deposited at a normal angle. The detailed analysis indicates that, (200) and (800) orientation are absent in the thin film grown at a glancing angle compared to the thin film grown at a normal angle, suggesting that the growth direction and orientation is not preferential. Moreover, there are many different grain orientations in the film, besides the common (201) and (311) peak, the sample deposited at a glancing angle has also (111) diffraction at 2θ = 30.5 °, (511) plane locates at 2θ = 49.73 °, (610) peak at a diffraction angle of 2θ = 52.47 ° and (420) orientation which is located at 2θ = 54.21 °. These orientations indicate that the thin films were not grown along *a* axis. There are such differences between the patterns of the two samples deposited at the normal and glancing angles, because the two films have distinct growth orientations and morphologies. A nanopillar structure is exhibited

on the film deposited at a glancing angle, and because there is difference between the diffraction at the tip of pillar and that on a plain film, the XRD patterns can be different. It should be noted that although the two films have different microstructures and crystal orientations, they possess the same crystal structure.

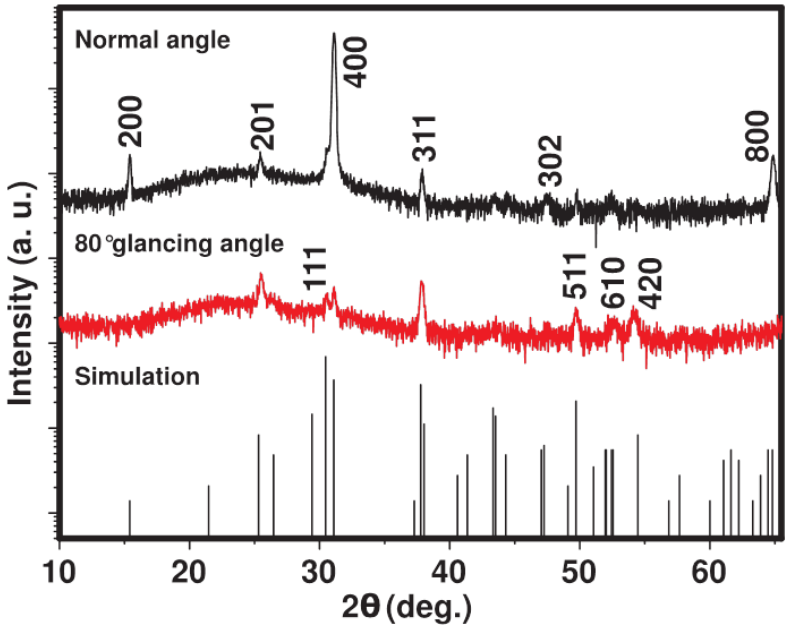

Figure 3.13. XRD patterns of the thin film deposited at a normal angle and an 80 ° glancing angle with T_s = 330 ℃. The patterns are compared to the SnSe simulation pattern (JCPDS #48-1224).

AFM and SEM were performed to study the thicknesses and surface morphologies of the SnSe thin films grown at glancing angle and normal angle. By conducting cross-sectional SEM, the thickness of the SnSe film deposited at a normal angle for a 30 minutes deposition is determined to be 730 nm, while for 60 minutes deposition, the film deposited at glancing angle is about 300 nm. This result indicates that deposition

rate for glancing angle deposition is much lower compared to that of the normal angle deposition. The morphologies of both films obtained by AFM are shown in Figure 3.14a and 3.14b. A comparison with SEM top view images can be made as shown in Figure 3.14c and 3.14d. In Figure 3.14a and 3.14c, the film deposited at a normal angle shows some local maximum points, in addition there are large grains nearby these maximum points. In contrast, from the top view images of the sample deposited at a glancing angle as shown in Figure 3.14b and 3.14d, a nanopillar structure rather than a continuous film on the substrate is shown. These nanopillars incline towards a specific direction, suggesting that the pillars grow towards the direction of the source flux during the deposition process[68-70]. Furthermore, the nanopillars grew in a relatively high density, in terms of grain size, the SnSe film deposited at a glancing angle has a grain size of ~120 nm with root-mean-square surface roughness (R_q) of 54 nm. Compared to that of film deposited at a normal angle which has an average grain size of ~730 nm with R_q of 17 nm, the grain size of the glancing angle deposited film has a six times smaller grain size, while at the same time, the film is more rough than the film deposited at normal angle. The morphology of the films can also be investigated by cross-sectional SEM, as shown in Figure 3.14e and 3.14f. In Figure 3.14e, it can be seen that the SnSe thin film deposited at normal angle exhibits a continuous columnar structure pointing upward, meanwhile there are many slanted nanopillars grow on the substrate surface for film deposited at the glancing angle. This result is well consistent with the top view images obtained by AFM and SEM. Through these detailed studies, it can be concluded that the films deposited at normal angle and glancing angle have very different morphologies and crystal orientations.

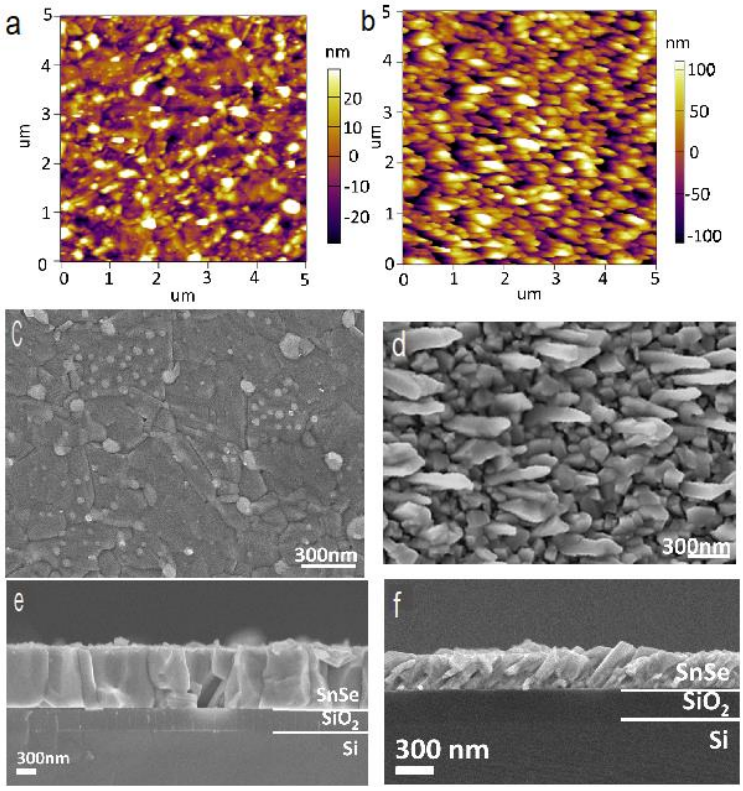

Figure 3.14. AFM images of SnSe thin films deposited at T_s = 330 ℃ at (a) normal angle and (b) glancing angle. Top view SEM images of films deposited at (c) normal angle and (d) glancing angle. Cross-sectional SEM images of films grown at (e) normal angle and (f) glancing angle.

3.4 TE property characterization of SnSe films deposited at normal angle and glancing angle

The Seebeck coefficients and electrical conductivities in in-plane direction, and the out-of-plane thermal conductivities of the thin films deposited at the normal and

glancing angle were obtained, and they are summarized in Figure 3.15.

From Figure 3.15a, one can see that both films show positive Seebeck coefficients, indicating a p-type semiconducting characteristic of the grown SnSe thin films. Moreover, both films exhibit a similar temperature dependence of Seebeck coefficients in temperatures ranging from 300 to 578 K. The Seebeck coefficient curves can be divided into two regions. In the first region, the Seebeck coefficients increase with the temperature, they reach their maximum at 477 and 426 K respectively, for the films deposited at normal and glancing angle. Specifically, the normal angle grown SnSe thin film exhibits a maximum Seebeck coefficient of 193.7 $\mu V/K$ at 477 K, while the maximum Seebeck coefficient of the film deposited at glancing angle is much higher, attaining 498.5 $\mu V/K$ at 426 K. After reaching the peak values, the Seebeck coefficients of the films start decreasing, and they converge in the second region reaching negative values at the highest measured temperature of ~579 K. The negative values obtained is due to the increasing intrinsic electron carrier concentration by thermal excitation according to the previous study[37].

Figure 3.15b shows the temperature dependence of electrical conductivity, where both the films show semiconducting characteristic. The electrical conductivities of the samples increase steadily from 300 to 426 K, while after 426 K, the two films are thermally activated such that the conductivities of them increase exponentially. These results are consistent to the drop of the Seebeck coefficients. Both of the electrical conductivities of the films deposited at normal angle and glancing angle show the same trend of temperature dependence, and are in the same order of magnitude. This indicates that there is no significant grain size effect on the electrical conductivity.

The comparison between the power factors of the SnSe thin film deposited at normal angle and glancing angle is shown in Figure 3.15c. The power factor of the film deposited at the glancing angle exhibits a maximum value of 18.5 $\mu W cm^{-1}K^{-2}$ at 478 K, which is more than 20 times higher than that of the film deposited at normal angle. The significant enhancement of power factor is mainly due to the increase of Seebeck coefficient, and the Seebeck coefficient improvement through the control of grain size can be explained by potential barrier scattering at grain boundaries. This concept has been theoretically and experimentally studied[36-38]. Assume a TE material only has one type of mobile charge carrier, the charge carriers will diffuse from the hot end to the cold end of the material if a constant thermal gradient is applied to the material, i.e., a Seebeck voltage is induced. On the other hand, on the two sides this Seebeck voltage induced potential difference will drive the charge carriers drift back to the original position and diminish the Seebeck voltage.

During the two competing process, if there is a potential barrier in the TE material, the drift of carrier can be retarded or even stopped, and therefore the Seebeck coefficient can be improved.

In this work, the grain boundaries act as potential barriers to scatter and filter the carriers, so that the carriers drifting from cold side to hot side possessing lower energy than the barrier can be stopped, while in the meantime the high energy carriers driven from hot side to cold side can pass through the barrier[76]. In the SnSe thin film grown at glancing angle, the surface area of grain boundary is increased, as a result, the low energy carriers can be effectively scattered, leading to an improvement of Seebeck coefficient. In addition, similar to the previous literature[36], there is a temperature

dependence of the grain size effect on the Seebeck coefficient. As shown in Figure 3.15a, there is a large difference between the Seebeck coefficients of the films deposited at normal angle and glancing angle at low temperatures. However, at higher temperatures beyond 426 K, they start to converge and the difference between them significantly reduced. This result suggests that at low temperatures, the mobile carriers do not have enough energy to overcome the potential barrier, so in the film deposited at the glancing angle, large amount of grain boundaries can effectively scatter the low energy carriers, leading to a large improvement of Seebeck coefficient. However at high temperatures, the carriers gain enough kinetic energy to pass through the grain boundaries, so the grain boundaries cannot hinder the carrier drift, resulting in little enhancement of Seebeck coefficient by increasing grain boundaries. Eventually the Seebeck coefficients of the two films converge at high temperature.

Figure 3.15d illustrates the temperature dependence of the out-of-plane thermal conductivities of the two SnSe thin films from 200 to 340 K. At temperatures ranging from 200 to 300 K, the film deposited at normal angle exhibits much higher thermal conductivity. While beyond 300 K, the thermal conductivities of them do not show a significant difference, but tend to the same value increasing with temperature. The thermal conductivities eventually attain the highest value of ~0.189 W/mK at 340 K. The trend of the thermal conductivities may be attributed to the low dimension of the thin films, so the thermal conductivity contributed by phonon is limited, and charge carrier density dominates the heat conduction. This leads to the increasing thermal conductivity as temperature increases.

In this work, the thermal conductivities of the films were measured in out-of-plane

direction, they cannot be directly used with those measured in-plane electrical properties. But they can be used as a reference to foresee the performance of those films. The thermal conductivities measured here does not cover the whole temperature range of other TE measurements, estimation can be made to reckon the actual performance of those SnSe films. Considering the increasing electrical conductivity of the SnSe film deposited at the glancing angle, the decreasing thermal conductivity of the bulk SnSe when temperature increases[59], and the expectation that the in-plane thermal conductivity will be lower than that in out-of-plane direction because of the nanopillar structure, it is conservative to estimate that the thermal conductivity of the glancing angle deposited film would constantly increase, and would reach 0.259 W/mK at 478 K. Based on this estimation the maximum zT of the SnSe film in this work can reach 3.4.

There were uncertainties in measuring the TE properties. For the 3 ω thermal conductivity measurement, 1% and 3% of error were introduced in measuring the dimensions of the metal line. 0.1% of uncertainty was produced in measuring the thickness of the thin film. The error in this measurement mainly came from the measurement of temperature change ΔT, which was estimated as 5%. Overall the uncertainty introduced in the 3ω was 5.7%. In measuring the Seebeck coefficient and electrical conductivity, 7% and 5% of uncertainties were introduced respectively.

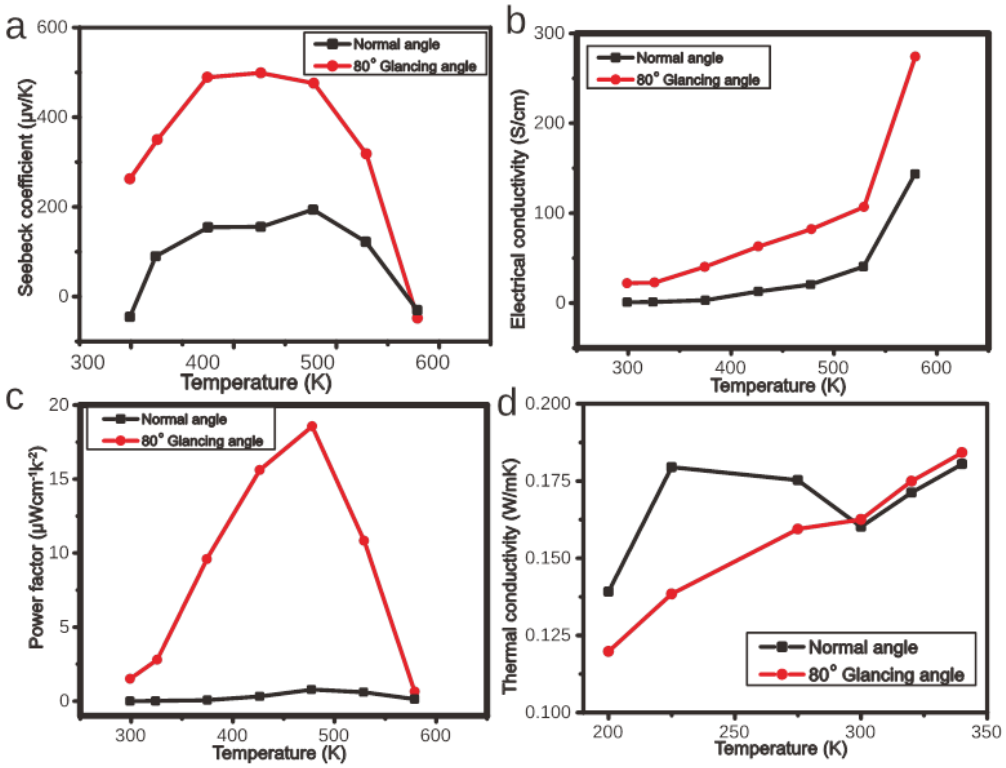

Figure 3.15. TE properties of SnSe thin films as a function of temperature. (a) Seebeck coefficient. (b) Electrical conductivity. (c) Power factor and (d) Thermal conductivity.

By comparing the TE performance of the as-deposited SnSe thin films with the bulk single crystal counterpart[59], one can see that the deposited films in this work have much lower operation temperature than that of the bulk material. Moreover, the out-of-plane thermal conductivities of the films deposited in this work have different trends compared to the SnSe single crystal. The bulk material has a decreasing thermal conductivity upon the increasing temperature. In addition, the thermal conductivities of the studied films are much lower than that of the bulk SnSe, it is believed that such observation should be due to the grain and surface boundary scattering presents in the

as-deposited thin films in this work. In terms of the figure of merit, the maximum zT in this work is estimated to be 3.4, which is higher than the bulk material of 2.6. Compared to the SnSe thin film deposited by the other group of researchers[41], the film deposited at a glancing angle has a lower Seebeck coefficient. In the previous study the room temperature Seebeck coefficient of SnSe films deposited on different substrates attained high values from 432 $\mu V/K$ to 505 $\mu V/K$, which is almost two times higher than the films in this work, with room temperature Seebeck coefficient of 262.2 $\mu V/K$.

3.5 Summary

Structural and TE property characterizations have been conducted on SnSe thin films deposited on NaCl and SiO_2/Si substrates. The results revealed that stoichiometric SnSe film can be deposited at an optimized temperature of 330 ℃. In contrast to the continuous columnar structure exhibited by the film deposited at normal angle, the film grown at glancing angle shows a slanted nanopillar structure with a smaller grain size. In TE measurements, the film deposited at glancing angle exhibits great enhancement of power factor for >20 times higher. The improvement of power factor is contributed by the increment of Seebeck coefficient, and it can be explained by the concept of energy barrier scattering effect. By comparing the thermal conductivities of the two films, the one deposited at normal angle has a higher thermal conductivity at relatively lower temperatures, which is consistent to the study of morphologies for the two films. With the presence of TE property enhancement, this study provides an

alternative strategy to boost the TE performance of thin films.

Chapter 4 Characterization of SnTe thin films and multilayered thin film composed of SnSe and SnTe

4.1 Introduction of Tin Telluride (SnTe)

SnTe has a simple cubic structure with space group of *Fm3m* (#225) adopting a face-centered structure. Figure 4.1 represents the schematic of SnTe crystal structure with a lattice constant of 0.63 nm. In terms of electronic band structure, SnTe has two valence bands (light-hole and heavy-hole bands) with band gap of 0.18 eV as shown in Figure 4.2. It has a similar crystal structure and band structure to PbTe, with difference of larger valence band offset of about 0.3 eV for SnTe compared to that of 0.1 eV for PbTe. This similarity suggests that SnTe has the potential to be a good TE material similar to PbTe, but without toxic Pb. However because of its low *zT* due to the low Seebeck coefficient and high electronic thermal conductivity, SnTe has been used for alloying material in other telluride systems for enhancing TE properties[77-89].

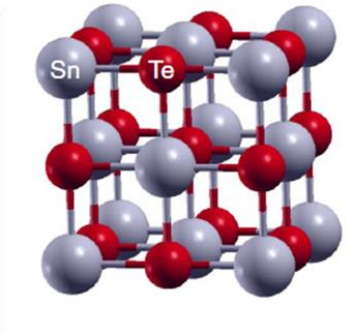

Figure 4.1. Crystal structure of cubic SnTe with lattice constant of 0.63 nm.

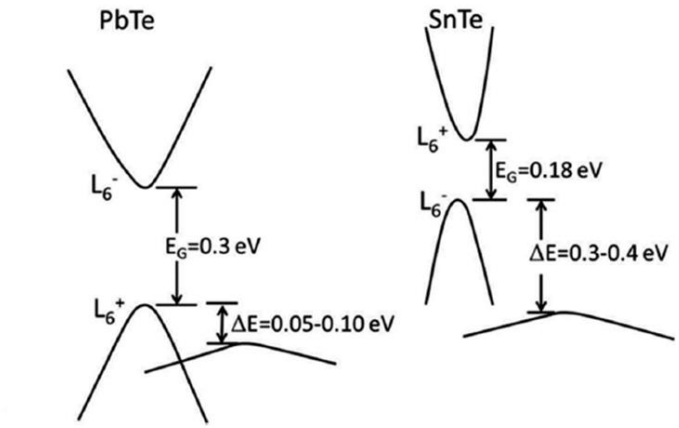

Figure 4.2. Simplified band structure of PbTe and SnTe.

Some groups of researchers worked on developing the SnTe system in TE field, and there were breakthroughs. Hoang *et al.*[90] have calculated the band structures of SnTe doped with monovalent (Na, K and Ag) and trivalent (Sb and Bi) impurities using supercell models. Based on the calculated band structures, they suggested that Ag- or Sb-doped SnTe systems should exhibit degenerate semiconducting or metallic conduction with a possibility of large Seebeck coefficient. Zhang *et al.*[91] also improved the TE properties of SnTe bulk material by small amount of indium (In) doping and

introduction of grain boundaries. With their fabricating process of high-energy ball milling and hot pressing which introduces grain boundaries, and reduces lattice thermal conductivity, they discovered that through doping, the *zT* can be improved from 0.7 to 1.1 when temperature is up to about 900 K. Zhou *et al.*[92] also investigated the effect of different doping to the TE properties, they decreased the carrier concentration by Iodine (I) doping and increased the carrier concentration of Gadolinium-doped or Te-deficient SnTe system experimentally. Their results suggest that the *zT*s are also enhanced for the both cases, but the improvement is more efficient for the I-doped SnTe system. Similar to the case as SnSe, the study of SnTe TE thin film was inadequate compared to the bulk SnTe. This arouses our interest to investigate the growth and TE properties of SnTe thin films.

4.2 Experimental Details

Similar to the procedures as mentioned in the previous chapter, the SnTe thin films were deposited on Si substrates with 300 nm of SiO_2 top layer at temperatures of 250 and 330 ℃. Multilayered thin film with SnSe was also deposited to study the effects of multilayered structure. The multilayered thin film was composed of 6 alternating layers of SnSe and SnTe, in which SnSe was the bottom layer. The layers were deposited at an interval of 10 minutes, between the intervals the deposition process stopped for no more than 1 minute so as to change the target, the substrate temperature in the deposition was less than the optimized temperature, so as to avoid the interfacial diffusion between the layers. All of the SnTe and multilayered films were deposited at

the normal angle. The crystal structure and TE properties of the as-deposited multilayered thin film were compared to those of the original SnTe thin film, the effects of the multilayered structure were investigated based on these results and are discussed in this chapter.

4.3 Structural characterization of SnTe and SnSe/SnTe multilayered films

The XRD patterns of the SnTe thin films deposited at 250 and 330 ℃ are shown in Figure 4.3. By adopting a cubic structure of SnTe (a = 0.63 nm, JCPDS #65-314), both films exhibit strong peaks at 2θ = 28.27 ° representing (200) plane. In addition other peaks also present in the pattern, such as (220), (400), weak (222) and (420) peak. It is apparent that the SnTe thin film deposited at 330 ℃ shows the strongest (200) and (400) peaks, and these two peaks are degraded in the film deposited at 250 ℃. These results indicate a worse crystallinity at relatively lower deposition temperature (250 ℃) compared to the SnTe film deposited at 330 ℃. To conclude, 330 ℃ is the best temperature for deposition SnTe.

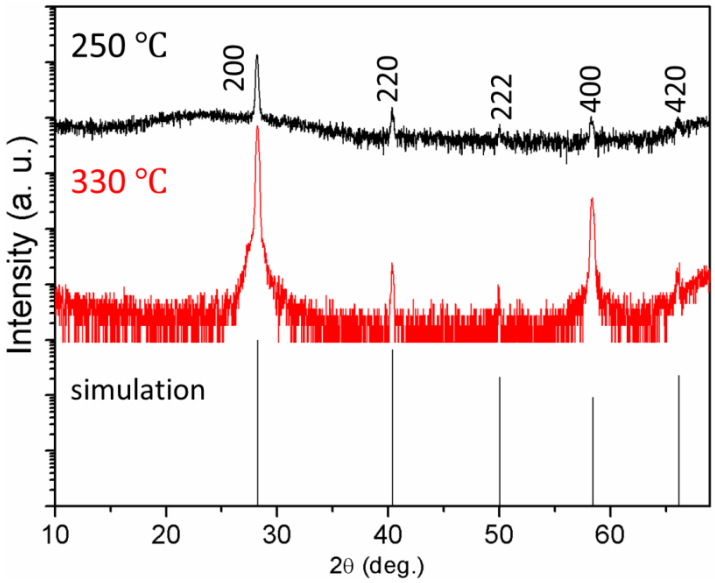

Figure 4.3. XRD patterns of the SnTe thin film deposited at 250 and 330 ℃. The patterns are compared to the SnTe simulation pattern (JCPDS #65-314).

To investigate the microstructure and composition of the SnTe thin film deposited at 330 ℃, TEM and EDX studies were conducted and the results are shown in Figure 4.4. The lattice spacing in Figure 4.4a matches the cubic SnTe (a = 0.63 nm) structure, and is consistent to the XRD results. The EDX spectrum as shown in Figure 4.4b displays the composition of SnTe thin film, with a ratio of Sn/Te = 1:1, indicating the stoichiometric SnTe compound of the film.

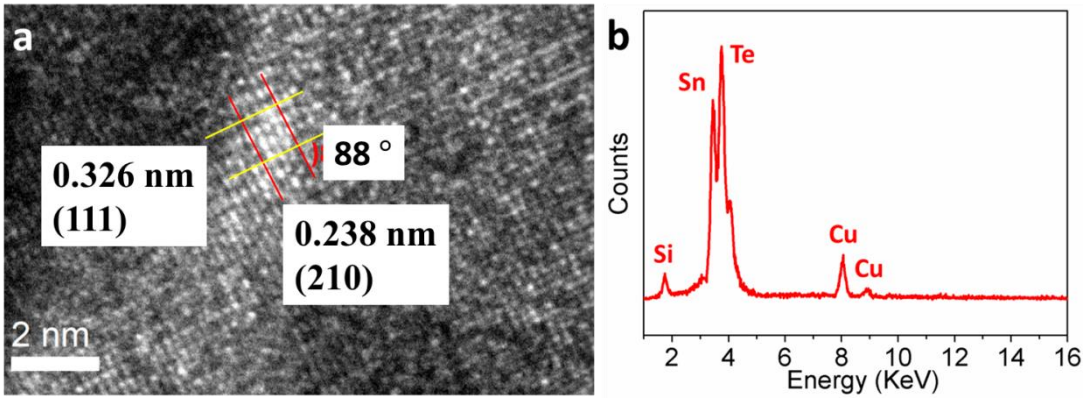

Figure 4.4. (a) HRTEM image showing (111) and (210) plane of SnTe with angle of 88 ° and (b) EDX spectrum of SnTe thin film deposited at substrate temperature T_s = 330 ℃. Si and Cu peaks are from substrate and Cu grid.

The thickness of the SnTe thin film deposited at T_s = 330 ℃ with a deposition time of 60 minutes is determined to be ~1.69 μm by cross-sectional SEM study as shown in Figure 4.5. It is apparent that the SnTe films has columnar structure, which is similar to the SnSe films deposited at a normal angle as shown in Figure 3.14e. One can also see that there are some humps on top of the film, suggesting a rough surface of the film. To study the morphology further, a top view of SEM was performed and the image is shown in Figure 4.6, where one can see that the film is flat in general but with small islands on the surface with diameters ranging from 1.8 to 13.6 μm. The formation of these islands can be explained by the defects introduced in thick films, i.e., as the film grows, defects and dislocations are introduced into the film. These defects perturb the normal growth of the film, and the defects stack together to form large defects, which should affect the quality of the film including the morphology.

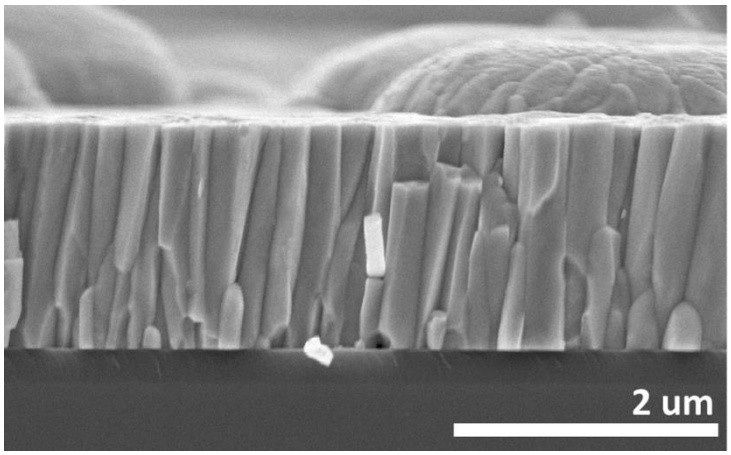

Figure 4.5. Cross-sectional SEM image of SnTe thin film with T_s = 330 ℃ and deposition time of 60 minutes.

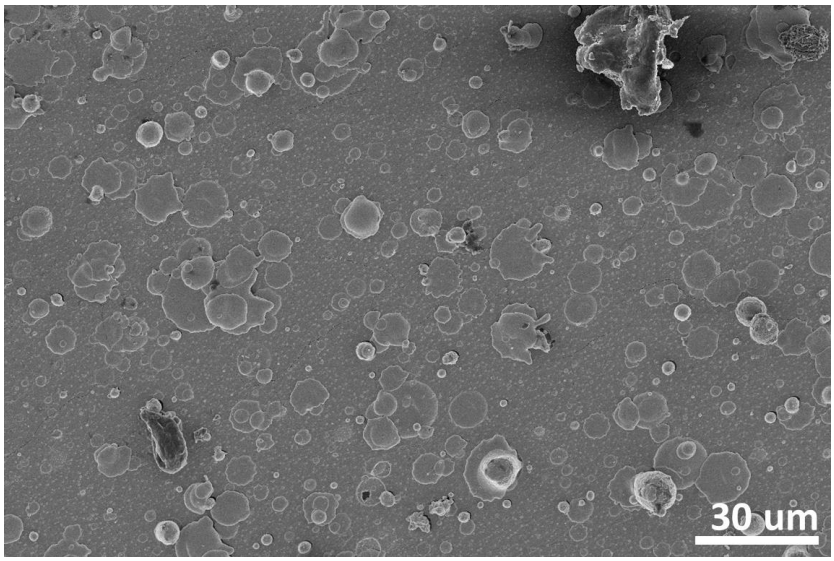

Figure 4.6. Top view SEM image of SnTe thin film deposited at 330 ℃, with a 60 minutes deposition time.

A multilayered SnSe/SnTe film was deposited by a similar condition to SnTe. After the substrate was preheated to 250 ℃, a SnSe layer was first deposited, with a deposition time of 10 minutes. After the SnSe deposition, a layer of SnTe with deposition time of

10 minutes was followed, and the deposition of SnSe and SnTe layers went back and forth until it reached 6 layers. The substrate temperature for the multilayer deposition was lower than the deposition temperature of SnSe and SnTe, because a lower substrate temperature can avoid the diffusion of atoms between the layers and prevent the formation of new phase in the film. Figure 4.7 shows the XRD pattern of such thin film with multilayered structure, the as-deposited film shows the characteristic peaks of SnSe and SnTe as mentioned in the previous sections, including (200), (400), (302) and (800) peaks of SnSe, and (200), (220) and (400) orientations of SnTe. By comparing the multilayered thin film with the SnSe film deposited at the normal angle with T_s = 250 ℃, they have most of the common peaks except (122) plane, suggests that (122) plane maybe developed in SnSe thick layer. As the SnSe film in the previous section has been deposited for 30 minutes, in this multilayered film, although the total deposition time of SnSe layers is also 30 minutes, they have been split into three separate layers, which reduce or even avoid the development of additional planes other than the preferential (200), (400) and (800) planes. By comparing the XRD patterns between the multilayered film and the SnTe thin film deposited at 250 ℃, it can be observed that the (222) and (420) plane diminish, also the peak of (400) orientation increases. Similar to the result of (122) plane in SnSe layers, the (220) peak of SnTe in multilayered film decreases compared to the SnTe original thin film, suggesting the suppression of (220) peak when the SnTe layers are thin. Overall the XRD pattern of the thin film with multilayered structure shows distinct peaks of SnSe and SnTe, suggesting little interfacial diffusion. The multilayered structure can be confirmed by investigating the cross-sectional SEM images of the multilayered thin film as shown

in Figure 4.8.

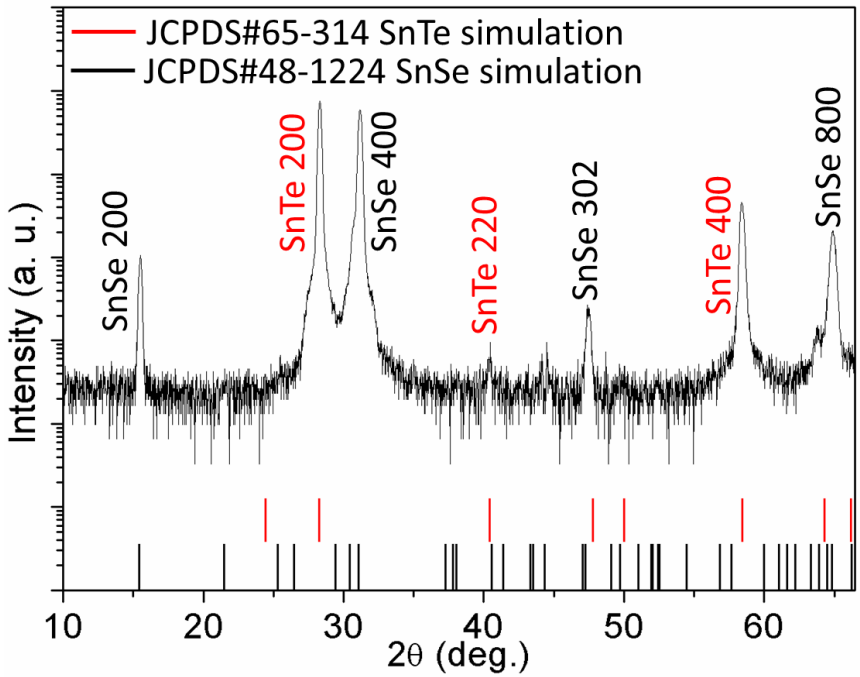

Figure 4.7. XRD pattern of the multilayered thin film consists of 6 layers of SnSe and SnTe deposited at 250 ℃.

With the help of the annotations, it can be obviously seen that the structure consists of 6 alternating SnSe and SnTe layers. The thicknesses of the 6 layers were measured and noted in the figure. One can see that for the layers of the same material, the thicknesses of them are not equal. For example the thicknesses of the SnSe layers vary throughout different deposition steps, from 202 nm to 187 nm then to 222 nm. The different thicknesses at different time interval may be due to the fact that during the deposition processes, the target was changed between SnSe and SnTe, as a result the laser spot position on the target during the SnSe deposition interval may not be the same as that at the previous SnSe deposition interval. This leads to an inconsistent deposition rate.

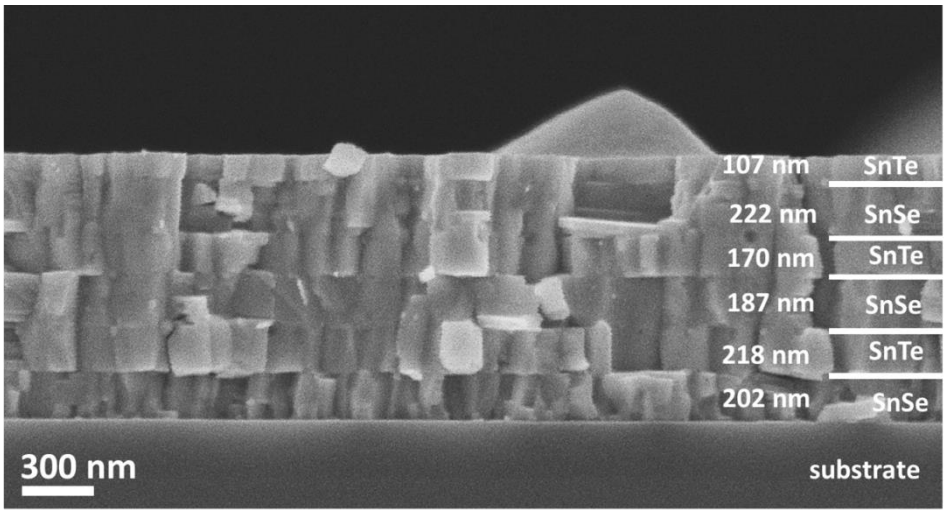

Figure 4.8. Cross-sectional SEM image of the multilayered thin film consists of 6 layers of SnSe and SnTe deposited at 250 ℃.

A cross-sectional TEM study was performed to examine the detailed structure of the multilayered thin film and the result is shown in Figure 4.9, where each layer can be identified and a structure with 6 layers can be observed. The thickness of each layer obtained by TEM is generally well consistent with that obtained by SEM.

A high-resolution TEM image from one of the SnTe layers is shown in Figure 4.10, where the (200) and (310) planes of SnTe can be identified.

The high-resolution TEM image of SnSe layer is shown in Figure 4.11. One can see that the SnSe layer is grown in high crystallinity even the deposition temperature is not at the optimized growth temperature.

High-resolution TEM image showing the atomically sharp interface between the SnSe and SnTe layers was also obtained as shown in Figure 4.12. It is obvious to see that there is a clear boundary between the two layers, indicating that the diffusion of the

two materials is greatly reduced by lowering the deposition temperature. In the SnTe layer, the (200) plane can be identified, while (111) and (200) planes are identified in the SnSe layer.

EDX analyses were conducted in all layers in the multilayered structure. The quantitative analysis results show stoichiometric SnTe and SnSe layers, indicating that interfacial diffusion between the SnSe and SnTe layers is very limited.

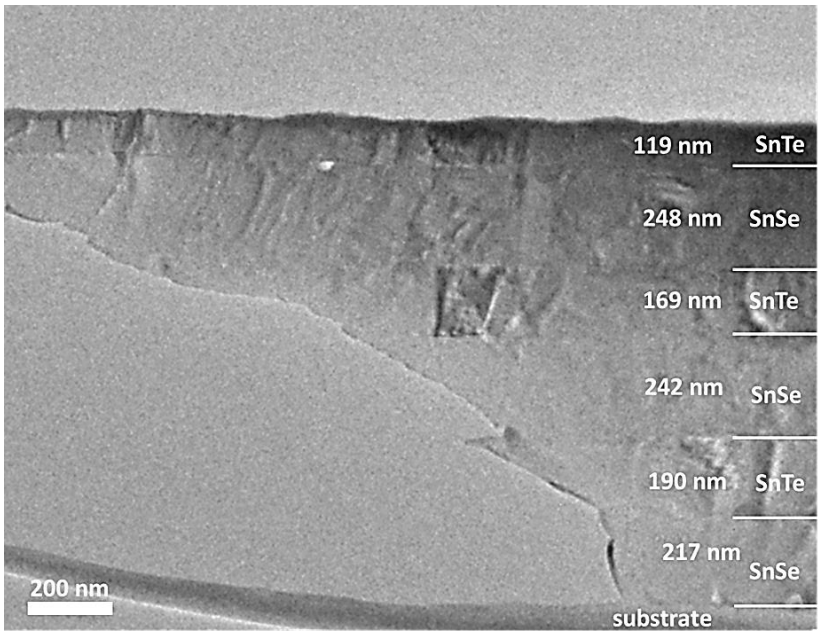

Figure 4.9. Cross-sectional TEM image of the multilayered thin film consists of 6 layers of SnSe and SnTe deposited at 250 ℃.

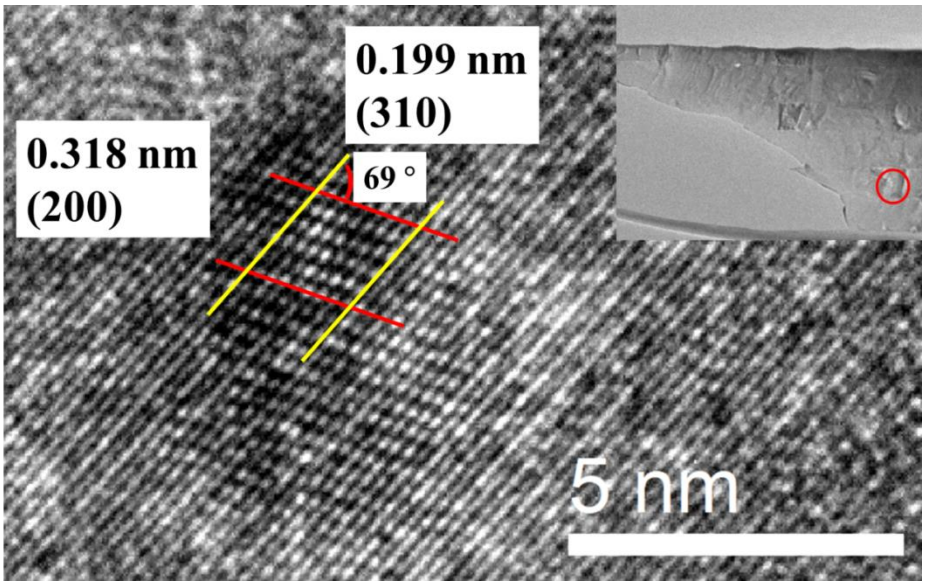

Figure 4.10. Cross-sectional TEM image of SnTe layer showing (200) and (310) planes with 69 °. Inset: The region where HRTEM was conducted.

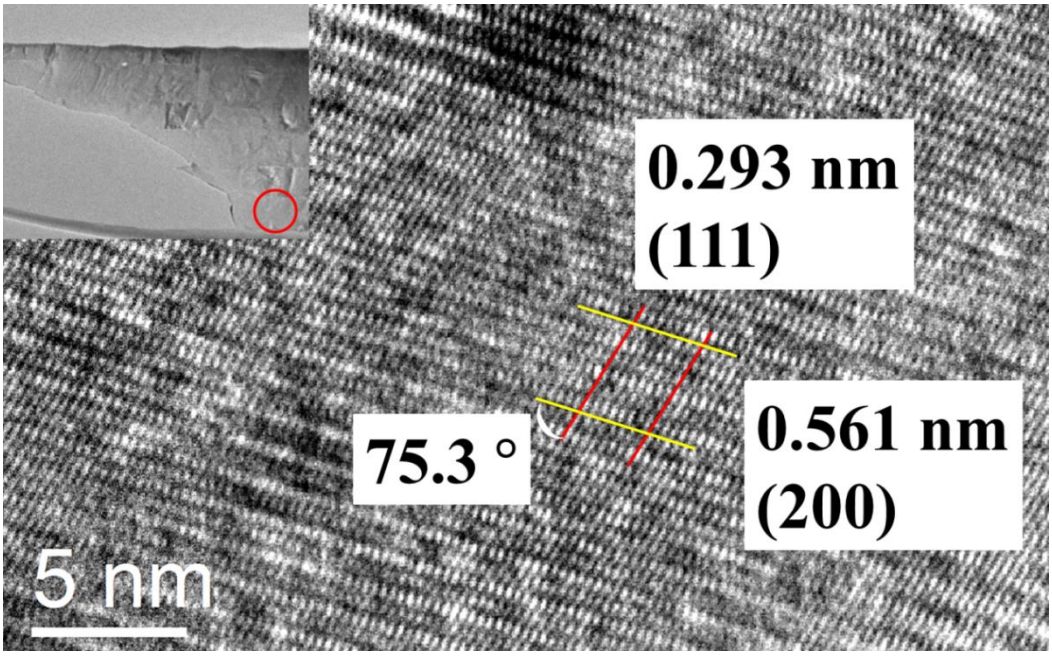

Figure 4.11. Cross-sectional TEM image showing (111) and (200) planes of SnSe layer with 75.3 °. Inset: The region where the HRTEM image was obtained.

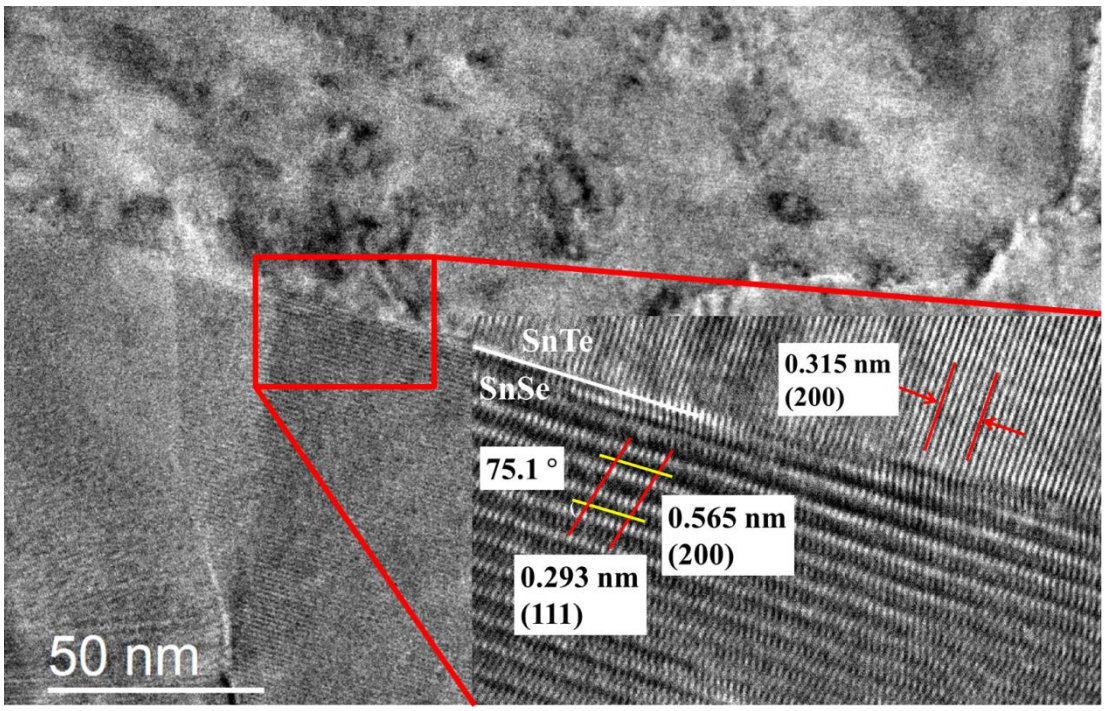

Figure 4.12. Cross-sectional TEM image showing the interface between SnSe and SnTe layers in the multilayered thin film. Inset: HRTEM image showing the (200) plane of SnTe, and (111) and (200) plane of SnSe. Between the two layers there is a clear boundary.

4.4 TE properties characterization of SnTe and SnSe/SnTe multilayered films

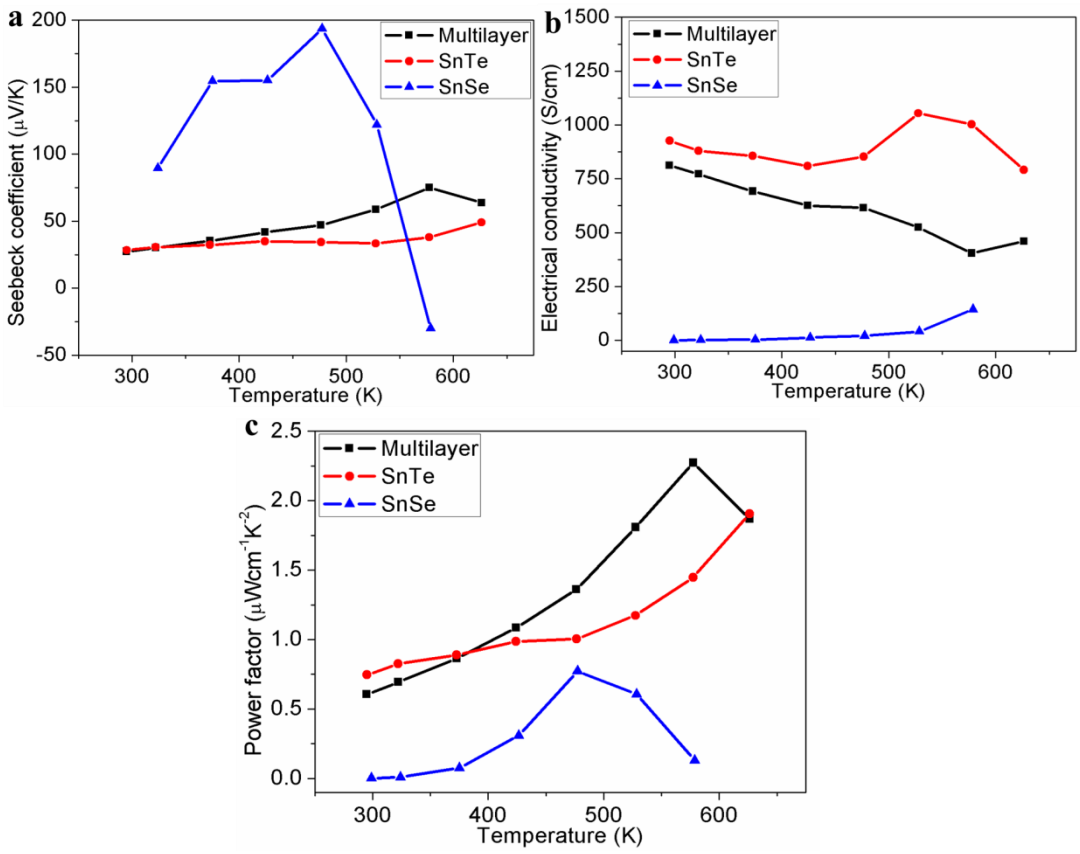

Figure 4.13. TE properties of the multilayered film, SnTe and SnSe thin films as a function of temperature. (a) Seebeck coefficient, (b) Electrical conductivity, and (c) Power factor.

The TE properties of the multilayered thin film were investigated, including its Seebeck coefficient, electrical conductivity and power factor. The properties of the original SnSe and SnTe thin films were also measured for comparison. All the three

thin films were deposited at normal angle.

By observing the Seebeck coefficients of the multilayered film and the SnTe film as shown in Figure 4.13a, one can see that they have room temperature Seebeck coefficients of almost 30 $\mu V/K$. When the temperature increases, the Seebeck coefficients increase with the temperature from room temperature to ~577 K. Throughout the temperature range, the thin film with multilayered structure shows a superior Seebeck coefficient over that of the SnTe film, in which the film with multilayered structure attains the maximum Seebeck coefficient of 75 $\mu V/K$ at a high temperature of 577 K, which is about 1.75 times of the Seebeck coefficient of the SnTe original film at the same temperature. This result suggests the carrier filtering at the boundaries between layers may enhance the Seebeck coefficient.

However the multilayered thin film does not show an enhanced Seebeck coefficient over the as-deposited SnSe film. The Seebeck coefficient of SnSe film is about 2.1 times as large of the multilayered film at 528 K. At 373K, the Seebeck coefficient of such SnSe thin film can even be 4.4 times larger compared with the multilayered structure. Within the temperature range of measurement, the Seebeck coefficient of the multilayered thin film can exceed that of the SnSe film only when temperature reaches about 579 K; at that temperature, the Seebeck coefficient of the original SnSe thin film is down to negative. By observing the temperature variation of the Seebeck coefficients, the examined multilayered thin film shows a similar trend as that of the SnTe film; both of them show monotonically increased Seebeck coefficients, in the temperature range from room temperature to 577 K. After 577 K, the Seebeck coefficient of the multilayered film starts decreasing, while the Seebeck coefficient of the as-deposited

SnTe film keeps increasing. In contrast to the similar trends mentioned, the examined multilayered film here shows a different temperature variation of Seebeck coefficient compared to that of the SnSe film. For the case of SnSe, the Seebeck coefficient first increases from the room temperature, until it reaches the maximum when the temperature is about 426 to 477 K. After that the Seebeck coefficient decreases. Other than the difference of temperature variation, the Seebeck coefficient of the thin film with multilayered structure has significantly smaller Seebeck coefficient than that of the SnSe thin film. In the measurement, the Seebeck coefficients were obtained in direction parallel to the surface of the substrates, meaning that the charge carriers diffuse along the in-plane direction when thermal gradient is applied. By introducing the grain boundaries as described in Chapter 3, the number of barriers increased in direction along the substrate plane, the carriers must pass through the barriers throughout the propagation, and this leads to a significant enhancement of Seebeck coefficient. By contrast, the introduction of multilayered structure as demonstrated here only increases the barrier in the direction perpendicular to the propagation of charge carriers, without greatly changing the in-plane barrier. Carriers in propagating the material are not necessary to pass through the layers, this may explain the less efficient enhancement of Seebeck coefficient by introducing multilayered structure, compared to the grain boundary introduction. However, the multilayered structure is expected to decrease thermal conductivity along the film thickness direction.

In terms of electrical conductivity, Figure 4.13b summarizes the temperature dependences of the electrical conductivities of the three thin films. For the SnTe thin film, the electrical conductivity shows a decreasing trend from about 900 to 800 S/cm

in the temperature range around 300 to 425 K, then it exhibits a semiconducting characteristic from ~425 to about 525 K; beyond that temperature the conductivity decreases again. Overall the as-deposited SnTe film shows a trend of decreasing electrical conductivity as the temperature increases, indicating a metallic behavior. The relatively higher electrical conductivity and metallic behavior of SnTe film can be explained by the narrower bandgap of SnTe which is about 0.18 eV compared to SnSe. Compared to the SnTe thin film, the film with multilayered structure has lower electrical conductivities in the whole temperature ranging from 300 to about 625 K, suggesting that the carrier can be scattered at interfaces between the SnSe and SnTe layers. The electrical conductivity of the studied film also shows a decreasing electrical conductivity variation with temperature, suggesting a metallic behavior of the as-deposited film. By contrast, the SnSe film exhibits an increasing electrical conductivity with increased temperature, showing a semiconducting behavior. Other than the difference between the trends, the electrical conductivity of the film with multilayered structure is higher than that of the SnSe film. At room temperature, the conductivity of 812 S/cm of the multilayered film is 1000 times greater than that of the SnSe film, even though SnSe has an increasing conductivity and multilayered film has a decreasing electrical conductivity, the conductivity of SnSe film is also 2.8 times smaller compared to that of the multilayered film, when temperature attains 578 K. Similar to the case of Seebeck coefficients, the electrical conductivity of the film with multilayered structure shows a similar trend as that of SnTe film, rather than that of the SnSe film. These results indicate that the TE property of the as-deposited film with multilayered structure is mainly contributed by the SnTe component.

The power factors (Figure 4.13c) of the SnSe, SnTe and multilayered thin films were derived from the Seebeck coefficient and electrical conductivity. It is apparent that the power factors of the multilayered and SnTe films show a similar temperature variation, in which they increase with the temperature. By comparison, the power factor of the film with multilayered structure increases gradually and it attains the maximum when the temperature reaches 577 K, which is about 1.5 times higher than the as-deposited SnTe film at that temperature. The enhancement of the power factor from the film with multilayered structure is attributed to the improvement of the Seebeck coefficient, as Seebeck coefficient has a larger contribution in the power factor compared to the electrical conductivity, although the multilayered film has a smaller electrical conductivity compared to the SnTe film. The enhancement of Seebeck coefficient also achieves a higher power factor; by comparing to the SnSe film, the multilayered thin film has a higher power factor than that of the SnSe film throughout the whole temperature range. Although SnSe film has a highest power factor of 0.77 $\mu W cm^{-1} K^{-2}$ at 477 K, the multilayered film has power factor for almost 2 times as large as that of the SnSe film. The reason of the higher power factor for multilayered thin film is due to the fact that the multilayered thin film has extremely higher electrical conductivity, which is up to 1000 times of SnSe film. So the film with multilayered structure has a higher power factor even though the SnSe film has significantly larger Seebeck coefficient.

The enhancement of TE properties by introducing a multilayered structure was proposed by Hicks *et al.*[5,6], they obtained the specific relationships between the quantum well width and the TE properties namely the Seebeck coefficient, electrical

conductivity and the thermal conductivity. A simulated figure of merit in relationship with the quantum well width was obtained and is shown in Figure 1.10. The proposal was also proved by different groups of researchers[24-27,93]. The idea of multilayered structure is that, assume the TE properties are studied along the direction of substrate surface, if a superlattice structure is introduced to a thin film, there is scattering between the layers, to both the carrier and phonon. However, as the interfaces are parallel to the propagation direction of the charge carriers, there is a small suppression in the transport of the electrical conductivity, leading to a limited conductivity decrease. In contrast, the interfaces between the layers scatter the phonon effectively, and lead to a significant decrease of thermal conductivity. In this work, as the thermoelectric properties of the multilayered film is mainly contributed by the SnTe component, there is no enhancement of Seebeck coefficient can be observed by introducing a multilayered structure over the SnSe film, the TE enhancement between them is only the electrical conductivity and possibly thermal conductivity.

By comparing the TE properties of the SnTe film with the bulk counterparts which are fabricated by the other researchers[92,94], our SnTe films has lower electrical conductivity compared to the bulk material fabricated by Freik et al,[94] but with a Seebeck coefficient doubled; so the power factor of the thin film in this work is higher. Compared to the work of Zhou's group, the electrical conductivity obtained from the SnTe thin film is about 2.5 times lower compared to the bulk material. Without any significant difference between the Seebeck coefficients of the film and the bulk SnTe, the power factor obtained from our thin film is lower than that of the SnTe bulk material.

4.5 Summary

The TE properties of the as-deposited SnSe and SnTe films have been obtained and compared to the multilayered film with six alternating layers of SnSe and SnTe. The multilayered thin film exhibits a superior Seebeck coefficient compared to that of the SnTe film. With a decrease of electrical conductivity, the enhancement of Seebcek coefficient and the degradation of electrical conductivity can be attributed to carrier scattering at interfaces between layers. Overall, the introduction of multilayer leads to a 1.5 times enhancement to the power factor. As a comparison to the studied SnSe film, the film with multilayered structure shows a degraded Seebeck coefficient, but a significant enhancement of electrical conductivity for 1000 times at room temperature. Power factor of the multilayered film is 1.7 times higher compared to the SnTe film. The temperature variations of Seebeck coefficient and electrical conductivity of the multilayered thin film show characteristics of SnTe rather than SnSe, indicating that the domination of SnTe properties in the multilayered thin film. The investigation in this work provides the feasibility on enhancing the thin film TE performances by introducing the multilayered structure.

Chapter 5 Conclusions

In this thesis work, two approaches to enhance the TE properties of SnSe and SnTe thin films have been investigated, namely the grain size reduction and multilayered structure. The grain size reduction is realized by a special deposition technique called pulsed-laser glancing angle deposition, and the multilayered structure is realized by alternating growth of the two layers. Structural and TE properties of those films are measured and compared to study the effect of the grain size reduction and multilayered structure.

For the grain size reduction, the SnSe thin film deposited at a glancing angle of 80 °, shows different crystal orientation compared to the SnSe film deposited at the normal angle. In addition, the film deposited at glancing angle shows a nanopillar structure pointing towards the source flux. The grain size of ~120 nm presented in the glancing angle deposited film had six times reduction compared to that of the normal angle deposited film. In terms of TE properties, the thin film deposited at a glancing angle shows a Seebeck coefficient of 498.5 $\mu V/K$ at 426 K, which is much higher than that of the film deposited at a normal angle. Without significant change of the electrical conductivity, the studied film attains a maximum power factor of 18.5 $\mu W cm^{-1} K^{-2}$, which is twenty times higher than that of the SnSe normal angle deposited film. The enhancement of the TE properties can be attributed to charge carrier scattering by grain boundaries.

By investigating the effect of multilayer approach, the distinct layers of SnSe and SnTe can be formed with limited interdiffusion. In TE measurements, the deposited thin film with multilayered structure exhibits a maximum Seebeck coefficient of

75 $\mu V/K$, which is 1.75 times as high as the SnTe thin film, but with a decrease of electrical conductivity. The power factor of the multilayered thin film is still 1.5 times as high as the SnTe thin film, and attains 2.25 $\mu W cm^{-1}K^{-2}$ at ~575 K. But the multilayered film shows an enhancement of electrical conductivity over the SnSe film instead of higher Seebeck coefficient. At 477 K, the power factor of the multilayered thin film is 1.7 times of that of the SnSe thin film.

These results demonstrate the enhancement of TE properties by reducing the grain size and introducing multilayered structure, providing alternative strategies on improving the TE performances of thin film thermoelectric materials.

5.1 Directions for Future Work

Even this work has achieved successful enhancements on the TE properties of thin film thermoelectric materials, the investigation can go further.

For example, the thermal conductivity of the thin films were measured in out-of-plane direction, the overall performance cannot be evaluated accurately with the in-plane electrical properties. To further investigate the thin films, the in-plane thermal conductivity should be measured.

Furthermore, the thin films should be made into TE devices, so that the enhanced TE properties can be confirmed in device scale.

References

1 Adminstration, U. S. E. I. Annual Energy Outlook 2017. (2017).

2 Pellergrino, J. L., Margolis, N., Justiniano, M. & Miller, M. Energy Use, Loss and Opportunities Analysis. (2004).

3 Moore, G. E. Cramming More Components onto Integrated Circuits. *Electronics*, 114-117 (1965).

4 Lin, S.-C. & Banerjee, K. Cool Chips: Opportunities and Implications for Power and Thermal Management. *IEEE Transactions on Electron Devices* **55**, 245-255 (2008).

5 Hicks, L. D. & Dresselhaus, M. S. Effect of quantum-well structures on the thermoelectric figure of merit. *Physical Review B* **47**, 12727-12731 (1993).

6 Hicks, L. D., Harman, T. C. & Dresselhaus, M. S. Use of quantum-well superlattices to obtain a high figure of merit from nonconventional thermoelectric materials. *Applied Physics Letters* **63**, 3230-3232 (1993).

7 Seebeck, T. J. Magnetic polarization of metals and minerals. *Abhandlungender Deutschen Akademie der Wissenschafrenzu Berlin* **265** (1822-1823).

8 Peltier, J. C. Nouvelles experiences sur la caloricite des courans electrique. *Ann. Chim.* **LV1**, 371 (1834).

9 Thomson, W. On a mechanical theory of thermoelectric currents. *Proceedings of the Royal Society of Edinburgh* **91** (1851).

10 da Silva, L. W., Kaviany, M., DeHennis, A. & Dyck, J. S. in *Proceedings ICT'03. 22nd International Conference on Thermoelectrics (IEEE Cat. No.03TH8726)* 665-668 (2003).

11 Snyder, G. J. & Toberer, E. S. Complex Thermoelectric Materials. *Nature Materials* **7**, 105-114 (2008).

12 Azar, K. & Tavassoli, B. TECs and Micro TECs for Spot Cooling Electronics. *Qpedia* **4**, 20-22 (2010).

13 Prasher, R. S. *et al.* Nano and Micro Technology-Based Next-Generation Package-Level Cooling Solutions. *Intel Technology Journal* **9**, 285-296 (2005).

14 Altenkirch, E. Uber den Nutzeffeckt der Thermosaule. *Physikalische*

Zeitschrifr **10** (1909).

15 Altenkirch, E. Electrothermische Kalteerzeugung and Reversible Electrische Heizung. *Physikalische Zeitschrifr* **12**, 920 (1911).

16 Bhushan, B. Handbook of nanotechnology. 345-373 (2007).

17 Pichanusakorn, P. & Bandaru, P. Nanostructured Thermoelectrics. *Materials Science and Engineering: R* **67**, 19-63 (2010).

18 Goldsmid, H. J. Applications of Thermoelectricity. (Methuen, London, 1960).

19 Zhang, X. & Zhao, L.-D. Thermoelectric materials: Energy conversion between heat and electricity. *Journal of Materiomics* **1**, 92-105 (2015).

20 Heremans, J. P. *et al.* Enhancement of Thermoelectric Efficiency in PbTe by Distortion of the Electronic Density of States. *Science* **321**, 554-557 (2008).

21 Wang, Q. Q. *et al.* Resonant distortion of electronic density of states and enhancement of thermoelectric properties of β-Zn_4Sb_3 by Pr doping. *Journal of Applied Physics* **113**, 124901 (2013).

22 Mahan, G. D. & Sofo, J. O. The best thermoelectric. *Proc. Natl. Acad. Sci. USA* **93**, 7436-7439 (1996).

23 Dresselhaus, M. S. *et al.* New Directions for Low-Dimensional Thermoelectric Materials. *Advanced Materials* **19**, 1043-1053 (2007).

24 Hicks, L. D., Harman, T. C., Sun, X. & Dresselhaus, M. S. Experimental study of the effect of quantum-well structures on the thermoelectric figure of merit. *Physical Review B* **53**, 493-496 (1996).

25 Koga, T., Cronin, S. B., Dresselhaus, M. S., Liu, J. L. & Wang, K. L. Experimental proof-of-principle investigation of enhanced $Z_{3D}T$ in (001) oriented Si/Ge superlattices. *Applied Physics Letters* **77**, 1490 (2000).

26 Venkatasubramanian, R. in Semiconductors and Semimetals: Recent Trends in Thermoelectric Materials Research III. 175-201 (2001).

27 Yang, B. & Chen, G. in Chemistry, Physics, and Materials Science for Thermoelectric Materials: Beyond Bismuth Telluride. 147-167 (2003).

28 Zhao, L. D. *et al.* Raising the thermoelectric performance of p-type PbS with endotaxial nanostructuring and valence-band offset engineering using CdS and ZnS. *J Am Chem Soc* **134**, 16327-16336 (2012).

29 Zhao, L. D. *et al.* High thermoelectric performance via hierarchical compositionally alloyed nanostructures. *J Am Chem Soc* **135**, 7364-7370 (2013).

30 Biswas, K. *et al.* High-performance bulk thermoelectrics with all-scale hierarchical architectures. *Nature* **489**, 414-418 (2012).

31 Zhao, L. D. *et al.* High performance thermoelectrics from earth-abundant materials: enhanced figure of merit in PbS by second phase nanostructures. *J Am Chem Soc* **133**, 20476-20487 (2011).

32 Ahn, K. *et al.* Exploring Resonance Levels and Nanostructuring in the PbTe-CdTe System and Enhancement of the Thermoelectric Figure of Merit. *J. Am. Chem. Soc.* **132**, 5227-5235 (2010).

33 Biswas, K. *et al.* High thermoelectric figure of merit in nanostructured p-type PbTe–MTe (M = Ca, Ba). *Energy & Environmental Science* **4** (2011).

34 Lee, Y. *et al.* High-performance tellurium-free thermoelectrics: all-scale hierarchical structuring of p-type PbSe-MSe systems (M = Ca, Sr, Ba). *J Am Chem Soc* **135**, 5152-5160 (2013).

35 Zhao, L.-D., Dravid, V. P. & Kanatzidis, M. G. The panoscopic approach to high performance thermoelectrics. *Energy Environ. Sci.* **7**, 251-268 (2014).

36 Gao, Y. W., He, Y. Z. & Zhu, L. L. Impact of grain size on the Seebeck coefficient of bulk polycrystalline thermoelectric materials. *Chinese Science Bulletin* **55**, 16-21 (2010).

37 Kuo, C. H. *et al.* Thermoelectric Properties of Fine-Grained PbTe Bulk Materials Fabricated by Cryomilling and Spark Plasma Sintering. *Materials Transactions* **52**, 795-801 (2011).

38 Takashiri, M. *et al.* Effect of grain size on thermoelectric properties of n-type nanocrystalline bismuth-telluride based thin films. *Journal of Applied Physics* **104**, 084302 (2008).

39 Valalaki, K., Vouroutzis, N. & Nassiopoulou, A. G. Significant enhancement of the thermoelectric figure of merit of polycrystalline Si films by reducing grain size. *Journal of Physics D: Applied Physics* **49**, 315104 (2016).

40 Yu, B. L., Qi, Q., Tang, X. F. & Zhang, Q. J. Effect of grain size on thermoelectric properties of $CoSb_3$ compound. *Chin. Phys. Soc.* **54**, 5763-5768 (2005).

41 Inoue, T., Hiramatsu, H., Hosono, H. & Kamiya, T. Heteroepitaxial growth of SnSe films by pulsed laser deposition using Se-rich targets. *Journal of Applied Physics* **118**, 205302 (2015).

42 Cahill, D. G. Thermal conductivity measurement from 30 to 750 K: the 3ω method. *Review of Scientific Instruments* **61**, 802-808 (1990).

43 Corbino, O. M. Measurement of specific heats of metals at high temperatures. *Atti della Reale Accademia Nazionale dei Lincei* **21**, 181-188 (1912).

44 Ebeling, H. Temperature variation in wires carrying alternating currents. *Annalen der Physik* **27**, 391-485 (1908).

45 Birge, N. O. & Nagel, S. R. Wide-frequency specific heat spectrometer. *Review of Scientific Instruments* **58**, 1464-1470 (1987).

46 Moon, I. K., Jeong, Y. H. & Kwun, S. I. The 3 omega technique for measuring dynamic specific heat and thermal conductivity of a liquid or solid. *Review of Scientific Instruments* **67**, 29-35 (1996).

47 Cahill, D. G. & Pohl, R. O. Thermal conductivity of amorphous solids above the plateau. *Physical Review B* **35**, 4067 (1987).

48 Bogner, M., Benstetter, G. & Fu, Y. Q. Cross- and in-plane thermal conductivity of AlN thin films measured using differential 3-omega method. *Surface and Coatings Technology* **320**, 91-96 (2017).

49 Chattopadhyay, T., Pannetier, J. & Von Schnering, H. G. Neutron diffraction study of the structural phase transition in SnS and SnSe. *J. Phys. Chem. Solids* **47**, 879-885 (1986).

50 Li, C. W. *et al.* Orbitally driven giant phonon anharmonicity in SnSe. *Nature Physics* **11**, 1063-1069 (2015).

51 Zhao, L.-D., Chang, C., Tan, G. & Kanatzidis, M. G. SnSe: a remarkable new thermoelectric material. *Energy Environ. Sci.* **9**, 3044-3060 (2016).

52 John, K. J., Pradeep, B. & Mathai, E. Tin selenide (SnSe) thin films prepared by reactive evaporation. *Journal of materials science* **29**, 1581-1583 (1994).

53 Sharma, J. *et al.* Preparation and characterization of SnSe nanocrystalline thin films. *Journal of Optoelectronics and Advanced Materials* **7**, 2085-2094 (2005).

54 Mariappan, R., Ragavendar, M. & Gowrisankar, G. Growth and characterization of SnSe thin films prepared by spray pyrolysis technique. *Chalcogenide Letters* **7**, 211-216 (2010).

55 Baummgardener, W. J., Choi, J. J., Lim, Y.-F. & Hanrath, T. SnSe Nanocrystals: Synthesis, Structure, Optical Properties, and Surface Chemistry. *J. Am. Chem. Soc.* **132**, 9519-9521 (2010).

56 Indirajith, R., Rajalakshmi, M., Gopalakrishnan, R. & Ramamurthi, K. Effects of Annealing on Thermally Evaporated SnSe Thin Films. *Ferroelectrics* **413**, 108-114 (2011).

57 Martínez-Escobar, D., Ramachandran, M., Sánchez-Juárez, A. & Narro Rios, J. S. Optical and electrical properties of $SnSe_2$ and SnSe thin films prepared by spray pyrolysis. *Thin Solid Films* **535**, 390-393 (2013).

58 Barrios-Salgado, E., Nair, M. T. S. & Nair, P. K. Chemically Deposited SnSe Thin Films: Thermal Stability and Solar Cell Application. *ECS Journal of Solid State Science and Technoogy* **3**, Q169-Q175, doi:10.1149/2.0131408jss] (2014).

59 Zhao, L.-D. *et al.* Ultralow thermal conductivity and high thermoelectric figure of merit in SnSe crystals. *Nature* **508**, 373-377 (2014).

60 Yu, H., Dai, S. & Chen, Y. Enhanced power factor via the control of structural phase transition in SnSe. *Sci Rep* **6**, 26193 (2016).

61 Duong, A. T. *et al.* Achieving ZT=2.2 with Bi-doped n-type SnSe single crystals. *Nat Commun* **7**, 13713 (2016).

62 Li, D. *et al.* Enhanced thermoelectric performance in n-type polycrystalline SnSe by PbBr2doping. *RSC Adv.* **7**, 17906-17912 (2017).

63 Zhou, M. *et al.* Thermoelectric performance of co-doped SnTe with resonant levels. *Applied Physics Letters* **109**, 042102 (2016).

64 Acosta, D. R., Magana, C. R., Martinez, A. I. & Maldonado, A. Structural evolution and optical characterization of indium doped cadmium sulfide thin films obtained by spray pyrolysis for different substrate temperatures. *Solar Energy Mater. Solar Cells* **82**, 11-20 (2004).

65 Bilgin, V., Kose, S., Atay, F. & Akyuz, I. The effect of substrate temperature on the structural and some physical properties of ultrasoniclly sprayed CdS films *Mater. Chem. Phys.* **94**, 103-108 (2005).

66 Ashour, A. Physical properties of spray pyrolysed CdS thin films. *Turk. J. Phys.* **27**, 551-558 (2003).

67 Patil, P. S., Sadale, S. B., Mujawar, S. H., Shinde, P. S. & Chigare, P. S. Synthesis of electrochromic tin oxide thin films with faster response by spray pyrolysis. *Applied Surface Science* **253**, 8560-8567 (2007).

68 Zhao, Y.-P., Ye, D.-X., Wang, G.-C. & Lu, T.-M. Designing Nanostructures by Glancing Angle Deposition. *Proceedings of SPIE* **5219**, 59-73 (2003).

69 Robbie, K. & Brett, M. J. Sculptured thin films and glancing angle deposition: Growth mechanics and applications. *Journal of Vacuum Science & Technology A: Vacuum, Surfaces, and Films* **15**, 1460-1465 (1997).

70 Wang, H. & Zhao, Y.-P. Nanostructure evolution of $YBa_2Cu_3O_x$ thin films

grown by pulsed-laser glancing-angle deposition. *J. Vac. Sci. Technol. B* **24**, 1230-1233 (2006).

71 Zhou, X. *et al.* Ultrathin SnSe2 Flakes Grown by Chemical Vapor Deposition for High-Performance Photodetectors. *Adv Mater* **27**, 8035-8041 (2015).

72 Cao, J. *et al.* Vertical SnSe nanorod arrays: from controlled synthesis and growth mechanism to thermistor and photoresistor. *Nanotechnology* **25**, 105705 (2014).

73 Hiramatsu, H., Ohta, H., Hirano, M. & Hosono, H. Heteroepitaxial growth of single-phase zinc blende ZnS films on transparent substrates by pulsed laser deposition under H_2S atmosphere. *Solid State Communications* **124**, 411-415 (2002).

74 Hiramatsu, H. *et al.* Mechanism for Heteroepitaxial Growth of Transparent P-Type Semiconductor: LaCuOS by Reactive Solid-Phase Epitaxy. *Crystal Growth & Design* **4**, 301-307 (2003).

75 Hiramatsu, H. *et al.* Opto-electronic properties and light-emitting device application of widegap layered oxychalcogenides: LaCuOCh(Ch= chalcogen) and La2CdO2Se2. *physica status solidi (a)* **203**, 2800-2811 (2006).

76 Suen, C. H. *et al.* Enhanced thermoelectric properties of SnSe thin films grown by pulsed laser glancing-angle deposition. *Journal of Materiomics* **3**, 293-298 (2017).

77 Gruzinov, B. F., Drabkin, I. A. & Zakomornaya, E. A. Electrical properties of $(PbSe)_{1-x}(SnTe)_x$ solid-solutions doped with In. *Sov. Phys. Semicond.* **15**, 190-193 (1981).

78 Androulakis, J. e. a. Spinodal decomposition and nucleation and growth as a means to bulk nanostructured thermoelectrics: Enhanced performance in Pb(1-x)Sn(x)Te-PbS. *J. Am. Chem. Soc.* **129**, 9780-9788 (2007).

79 Arachchige, I. U. & Kanatzidis, M. G. Anomalous band Gap evolution from band in-version in $Pb_{1-x}Sn_xTe$ nanocrystals. *Nano. Lett.* **9**, 1583-1587 (2009).

80 Shi, X., Salvador, J. R., Yang, J. & Wang, H. Prospective thermoelectric materials: $(AgSbTe_2)_{100-x}(SnTe)_x$ quaternary system (x = 80, 85, 90 and 95). *Sci. Adv. Mater.* **3**, 667-671 (2011).

81 Han, M. K., Androulakis, J., Kim, S. J. & Kanatzidis, M. G. Lead-free thermoelectrics: High figure of merit in p-type $AgSn_mSbTe_{m+2}$. *Adv. Energy Mater.* **2**, 157-161 (2012).

82 Chen, Y. e. a. SnTe-AgSbTe2 thermoelectric alloys. *Adv. Energy Mater.* **2**

(2012).

83 Nasirov, Y. N. & Feiziev, Y. S. Effect of small substitutions of tin by neodymium on thermoelectric properties of SnTe. *Phys. Status Solidi* **24**, K 157-K 159 (1967).

84 Nasirov, Y. N., Sultanova, N. P. & G., O. T. Thermoelectric properties of solid solutions based on SnTe-A^{11}Te-type tin telluride. *Phys. Status Solidi* **35**, K 39-K 42 (1969).

85 Sultanova, N. P., Nasirov, Y. N., I., Z. M. & Pirzade, M. M. Thermoelectric properties of a solid solution of the system SnTe-ZnTe. *Inorg. Mater.* **10**, 1219-1221 (1974).

86 Rustamov, P. G., Alidzhanov, M. A. & N., B. Y. The system SnTe-Tl_2Te_3. *Inorg. Mater.* **12**, 715-717 (1976).

87 Bushmarina, G. S., Gruzinov, B. F., Drabkin, I. A., Lev, E. Y. & Yuneev, V. M. Characteristics of the effects of In as a dopant in SnTe. *Sov. Phys. Semicond.* **18**, 1374-1377 (1984).

88 Vedeneev, V. P., Krivoruchko, S. P. & Sabo, E. P. Tin telluride based thermoelectrical alloys. *Semicond.* **32**, 241-244 (1998).

89 Asadov, M. M., Alidzhanov, M. A., Mamedov, F. M. & Kelbaliev, G. I. Electrical conductivity and thermoelectric power of SnTe-based alloys doped with Fe. *Inorg. Mater.* **34**, 442-444 (1998).

90 Hoang, K., Mahanti, S. D. & Kanatzidis, M. G. Impurity clustering and impurity-induced bands in PbTe-, SnTe-, and GeTe-based bulk thermoelectrics. *Physical Review B* **81**, 115106 (2010).

91 Zhang, Q. *et al.* High thermoelectric performance by resonant dopant indium in nanostructured SnTe. *Proc Natl Acad Sci U S A* **110**, 13261-13266 (2013).

92 Zhou, M. *et al.* Optimization of thermoelectric efficiency in SnTe: the case for the light band. *Phys Chem Chem Phys* **16**, 20741-20748 (2014).

93 Tan, M., Deng, Y. & Hao, Y. Enhanced Thermoelectric Properties and Superlattice Structure of a Bi_2Te_3/ZrB_2 Film Prepared by Ion-Beam-Assisted Deposition. *j. Phys. Chem. C* **117**, 20415-20420 (2013).

94 Freik, D. M. *et al.* Thermoelectric Properties of Bismuth-Doped Tin Telluride SnTe:Bi. *Ukrainian Journal of Physics* **61**, 155-159 (2016).